EarthArXiv Preprint

GEM-15: Global surface and terrain elevation models (15 meters) from sub-meter optical stereo imagery

Vishal Batchu[1], Maxim Neumann[2], Tommy Li[3], Brett Allen[3], Jie Zhang[3], and Christopher Van Arsdale[1]

[1]Google Research, Mountain View, CA 94043, USA
[2]Google DeepMind, Zurich, 8002, Switzerland
[3]Google, Mountain View, CA 94043, USA

Emails: vishalbatchu@google.com, maximneumann@google.com, litommy@google.com, brettallen@google.com, jiezh@google.com, cvanarsdale@google.com

Submitter ORCID: https://orcid.org/0000-0003-0461-0730

Peer review status: This is a non-peer-reviewed preprint submitted to EarthArXiv.

This manuscript has been submitted for peer review in *Earth System Science Data* (ESSD). Please note that the manuscript has yet to be formally accepted for publication. Subsequent versions of this manuscript may have slightly different content. If accepted, the final peer-reviewed version of this manuscript will be available via the "Peer-reviewed Publication DOI" link on the right-hand side of the EarthArXiv webpage. Please feel free to contact any of the authors; we welcome feedback.

GEM-15: Global surface and terrain elevation models (15 meters) from sub-meter optical stereo imagery

Vishal Batchu[1], Maxim Neumann[2], Tommy Li[3], Brett Allen[3], Jie Zhang[3], and Christopher Van Arsdale[1]

[1]Google Research, Mountain View, CA 94043, USA
[2]Google DeepMind, Zurich, 8002, Switzerland
[3]Google, Mountain View, CA 94043, USA

Correspondence: Vishal Batchu (vishalbatchu@google.com)

Abstract. Existing open global digital elevation models (DEMs) are limited to 30 m resolution, blur fine-scale urban and canopy structure, and rely on satellite missions flown between 2000 and 2015. We present Google's Global Elevation Models at 15 m (GEM-15), to our knowledge the first openly available near-global multi-layer elevation dataset at 15 m grid spacing. GEM-15 aggregates native 0.5 m optical stereo reconstructions acquired through 2024 (63.2 % of mapped tiles primarily from 2022–2024 30 cm Pléiades Neo imagery) and provides four times the spatial sampling density of 30 m baselines, more current representation of the Earth's surface, and higher vertical accuracy over complex canopies, buildings, and steep relief. Alongside the primary 15 m digital surface model (DSM), GEM-15 includes within-cell elevation percentiles (P_5, P_{50}, P_{95}), local elevation standard deviation (DSM σ_z), and a co-registered 15 m bare-earth digital terrain model (DTM) to capture within-cell 3D structure. We evaluate GEM-15 alongside the open 30 m DEMs Copernicus GLO-30, ALOS AW3D30, NASADEM and, for the terrain model, FABDEM against spaceborne GEDI lidar, 12 airborne and drone lidar benchmarks, and 4 071 GNSS CORS stations. Across the lidar benchmarks, the GEM-15 DSM has a 12.3 % lower mean tile-debiased root-mean-square error (DRMSE) than Copernicus GLO-30 (3.37 m vs. 3.85 m), rising to 13.7 % (3.69 m vs. 4.27 m) for the seven benchmarks with acquisition midpoints from 2021 onward; the margin increases with the reference survey date (Spearman $\rho = 0.87$ across the 10 non-rainforest campaigns) and reaches 27 % for the 2024–2025 New Zealand survey. The co-registered DTM is comparable in accuracy to FABDEM in open terrain and less accurate beneath closed canopy. In repeat surveys at US NEON sites, the 30 m DEMs diverge increasingly from recent lidar, whereas GEM-15 has the lowest DRMSE in every year. The dataset is available under a CC BY 4.0 license at https://developers.google.com/earth-engine/datasets/catalog/projects_climate-and-sustainability_assets_gem-15_v1.

1 Introduction

Digital elevation models (DEMs) form the topographic baseline for quantitative Earth system modeling and environmental management. In hydrology, elevation data govern watershed delineation, river-network extraction, and flood-inundation modeling (Lehner et al., 2008; Sampson et al., 2015), while also serving as essential inputs for forest biomass and carbon accounting (Dubayah et al., 2020), landslide susceptibility mapping, infrastructure planning, and coastal vulnerability assessments under rising sea levels (Reichenbach et al., 2018; Kulp and Strauss, 2019). The usefulness of a global elevation dataset for these appli-

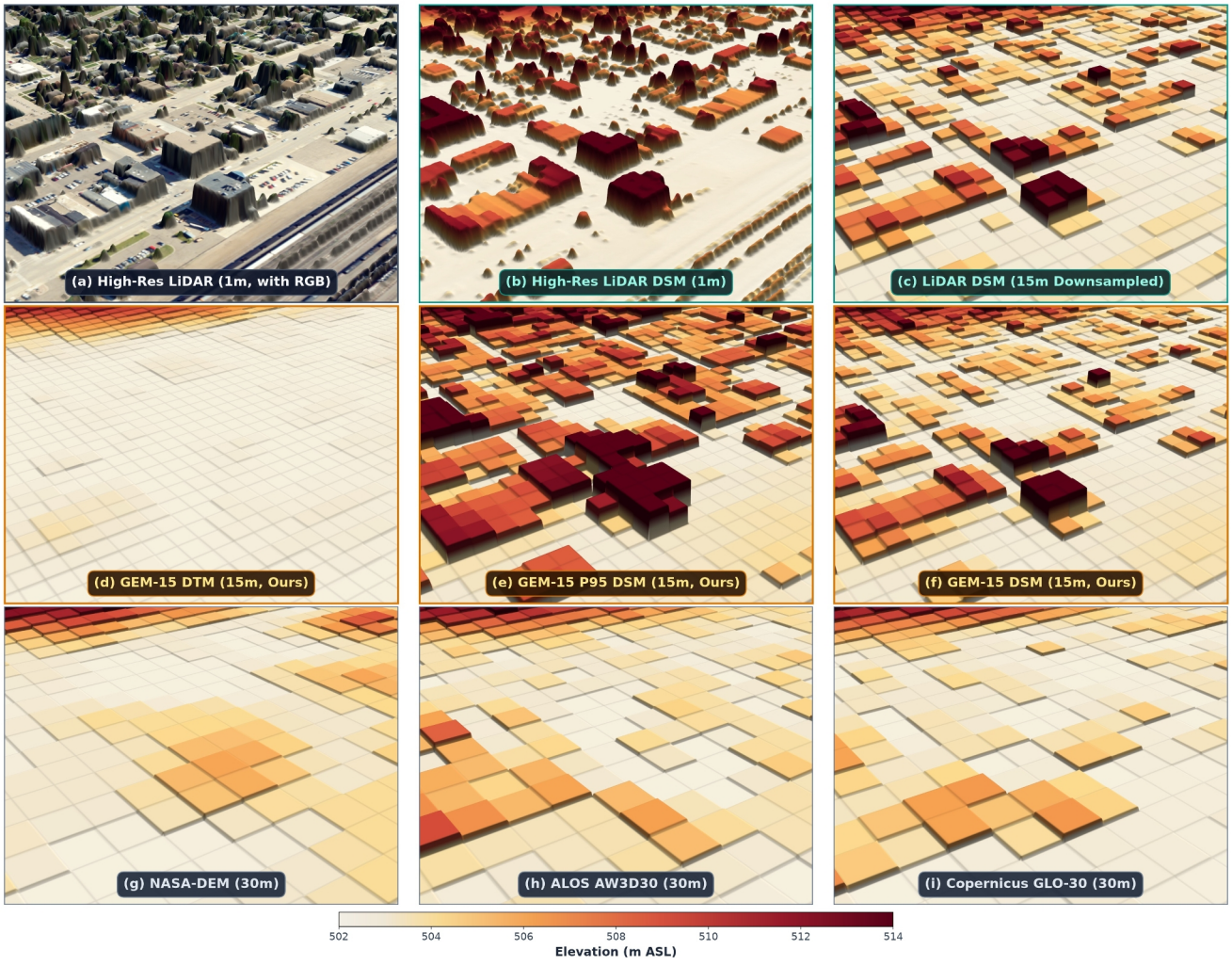


Figure 1. 2.5D surface rendering over downtown Mandan, North Dakota, comparing (a, b) native 1 m airborne lidar reference data and (c) 15 m aggregated lidar DSM against (d) GEM-15 DTM (15 m), (e) GEM-15 P_{95} DSM (15 m), (f) GEM-15 mean DSM (15 m), and 30 m global DEM baselines: (g) NASADEM, (h) ALOS AW3D30, and (i) Copernicus GLO-30. All structures in the scene predate the ALOS AW3D30 and Copernicus GLO-30 acquisitions (only NASADEM partially predates the northernmost complex), demonstrating that the missing and attenuated buildings in the 30 m baselines arise from resolution limits and sensor smoothing rather than temporal change.

cations depends on four factors: its effective horizontal resolution, its vertical accuracy, how closely its underlying observations reflect present-day landscapes, and whether it can separate above-ground canopy and built structures from the bare-earth terrain beneath them.

Open global elevation mapping began with the Shuttle Radar Topography Mission (SRTM) in February 2000, which used single-pass C-band interferometric synthetic aperture radar (InSAR) to map 80 % of the Earth's landmass between 56° S and

60° N (Farr et al., 2007). Subsequent reprocessing of the original SRTM radar returns yielded NASADEM, which had improved phase unwrapping and height-ripple error corrections calibrated against ICESat Geoscience Laser Altimeter System (GLAS) ground control points (Schutz et al., 2005; Zwally et al., 2002; Crippen et al., 2016; NASA JPL, 2020). The ALOS World 3D 30 m model (AW3D30) was derived from optical stereo imagery collected by the PRISM sensor between 2006 and 2011, where masking cloud, snow, and water outliers is a primary processing challenge (Takaku et al., 2014; Tadono et al., 2015). Large-area open DEMs have also been produced by automated multi-view stereo from commercial satellite imagery by the Polar Geospatial Center (PGC) using the SETSM algorithm (Noh and Howat, 2015), notably ArcticDEM (Porter et al., 2018), and REMA (Howat et al., 2019). The Copernicus GLO-30 DEM (European Space Agency, 2022) is based on X-band InSAR data acquired by the TanDEM-X (Krieger et al., 2007) mission between 2011 and 2015. Owing to its lower error over bare ground, GLO-30 has become the standard baseline for global terrain analysis (Rizzoli et al., 2017; Bielski et al., 2024). A global comparison against ICESat, GEDI, and ICESat-2 lidar showed that vertical accuracy improved from SRTM to NASADEM and GLO-30 (Simard et al., 2024).

At 30 m grid spacing, with potentially even coarser underlying resolution, fine-grained features such as individual buildings, street corridors, narrow drainage channels, road embankments, and forest edges are smoothed into gradual ramps. By contrast, aggregating native sub-meter stereo reconstructions directly to a 15 m grid retains structural detail, such as individual buildings and street corridors, that is also present in airborne lidar reference data (Fig. 1). Equally important, the satellite observations behind SRTM, AW3D30, and GLO-30 were all collected between 2000 and 2015 and are now more than a decade old. Because landscapes are continually modified by urban expansion (Seto et al., 2012), agricultural grading, deforestation (Hansen et al., 2013), and open-pit mining (Maus et al., 2020), static elevation models from the 2000s and early 2010s no longer capture present-day topography in rapidly changing regions. This time gap also complicates empirical validation: when a modern elevation dataset is benchmarked against older airborne lidar, landscape changes over the intervening years register as elevation errors, whereas evaluating legacy DEMs against benchmarks from their own mission eras hides their loss of accuracy on current landscapes.

Conventional global elevation products typically provide only a single digital surface model (DSM) value per grid cell, which averages vegetation canopies, building rooftops, and bare ground into one composite height. Post-processing efforts such as MERIT DEM at 90 m (Yamazaki et al., 2017), as well as FABDEM (Forest And Buildings removed Copernicus DEM; Hawker et al. 2022) and GEDTM30 (Ho et al., 2025) at 30 m, use statistical filtering or machine learning to subtract estimated canopy and building heights from existing DSMs to approximate a bare-ground digital terrain model (DTM). However, because these corrections are applied to 30 m DSMs, they cannot resolve ground and above-ground structure within a 30 m cell. Estimating the terrain from surface geometry that is first resolved at sub-meter scale, before aggregation to the output grid, can in principle preserve sharper terrain boundaries (Sithole and Vosselman, 2004; Gevaert et al., 2018); we examine this on steep slopes (Sect. 4.2.2) and along a stream corridor (Sect. 5.2).

Here, we introduce Google's Global Elevation Models at 15 m resolution (GEM-15), an open near-global elevation dataset (Sect. 2.1) generated from multi-view sub-meter optical stereo imagery acquired until 2024, predominantly 30 cm Pléiades Neo observations collected in 2022–2024 (Sect. 2.2). At the core of GEM-15 is a 15 m DSM produced by aggregating quality-

screened 0.5 m stereo reconstructions. Alongside the mean surface elevation, each 15 m grid cell includes sub-cell vertical percentiles (P_5, P_{50}, P_{95}), local elevation standard deviation (DSM σ_z), and a co-registered 15 m bare-earth DTM inferred from high-resolution DSM and optical imagery inputs using a convolutional neural network. To our knowledge, no open global elevation product has so far provided within-cell height percentiles, sub-cell standard deviation, and a co-registered bare-earth terrain model on a common grid; such statistics have previously been available mainly from airborne lidar or, for vegetation only, from single-variable canopy height maps (Potapov et al., 2021; Lang et al., 2023; Tolan et al., 2024). We evaluate the dataset across three independent reference suites: global spaceborne lidar waveforms from GEDI, 12 airborne and drone lidar benchmarks from different countries, and 4071 continuously operating Global Navigation Satellite System (GNSS) reference stations (CORS) distributed across six continents. We compare GEM-15 against Copernicus GLO-30, ALOS AW3D30, and NASADEM on these benchmarks, and use repeated lidar benchmarks over fixed cohorts of US National Ecological Observatory Network (NEON) sites between 2016 and 2025 to separate the effect of landscape change since the 2000–2015 baseline acquisitions from regional differences between benchmarks.

2 Data

In this section, we describe the GEM-15 product suite (Sect. 2.1), the satellite stereo imagery from which it is generated (Sect. 2.2), the global elevation models used as baselines (Sect. 2.3), and the independent reference datasets compiled for validation (Sect. 2.4).

2.1 GEM-15 dataset

The GEM-15 dataset provides co-registered digital surface models (DSMs), sub-grid-cell elevation percentiles (P_5, P_{50}, P_{95}), local elevation standard deviation (DSM σ_z), and bare-earth digital terrain models (DTMs) at 15 m horizontal grid spacing globally, covering the large majority of the ice-free land surface outside Russia, China, Mongolia, and Greenland, where commercial licensing restrictions preclude suitable source imagery (Fig. 2; Sect. 2.1.3). In addition, localized regions and cells are masked out where water bodies, stereo errors, or low-texture planar artifacts degrade reconstruction fidelity, as detailed in Sect. 3.1.2.

2.1.1 Digital surface model (DSM) layers

To represent both the mean surface elevation and the sub-grid-cell vertical distribution of vegetation canopies and built structures within each $15\,\mathrm{m} \times 15\,\mathrm{m}$ grid cell, the DSM product comprises five co-registered elevation and structural layers (all expressed in m). The primary layer is the block-mean surface model (DSM), computed as the mean of all unmasked 2.5 m sub-cells (bilinearly resampled from the native 0.5 m DSM; Sect. 3.1.2) within each 15 m cell. This layer captures the uppermost visible surface features, including buildings and vegetation canopies.

To capture the vertical structure within each 15 m grid cell that would otherwise be lost during spatial averaging, GEM-15 also includes three within-cell elevation percentiles: DSM P_5, P_{50}, and P_{95}. In semi-open woodlands and urban corridors, the

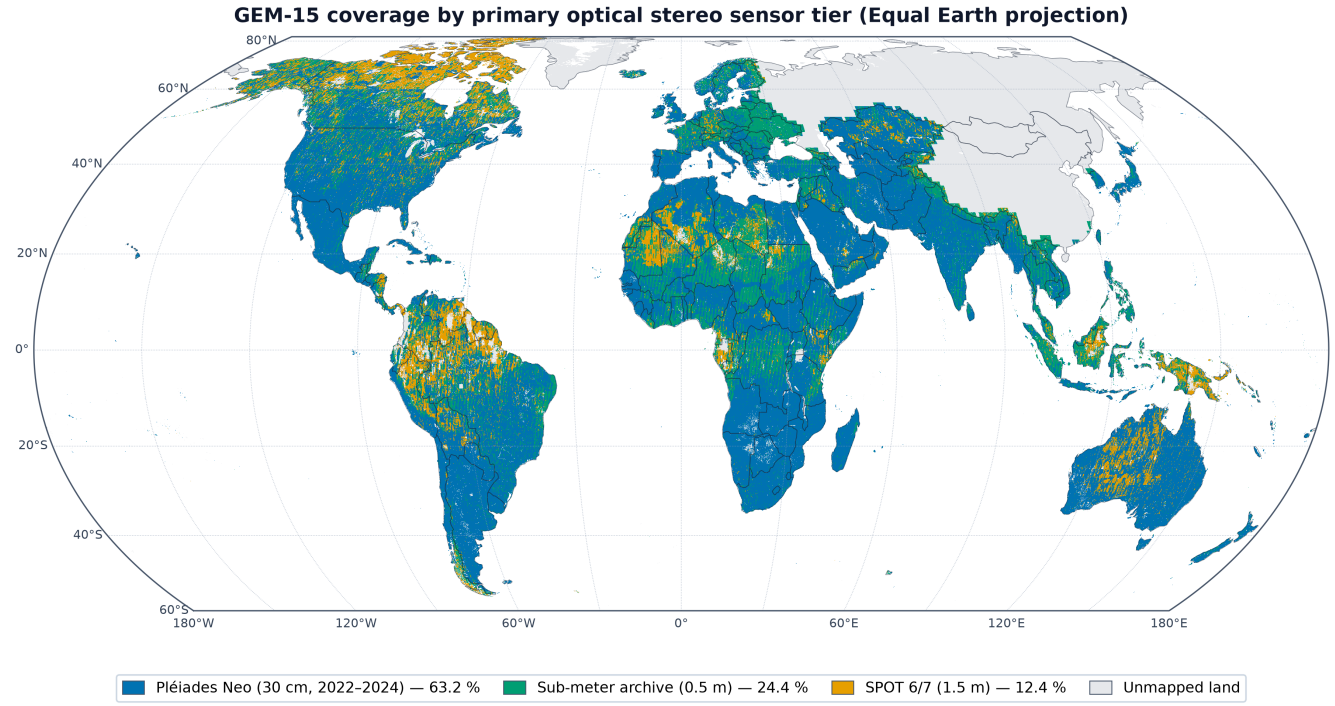


Figure 2. Global tile coverage of GEM-15 colored by primary optical stereo sensor tier: Pléiades Neo 30 cm (blue), sub-meter archive constellations (green), and SPOT 6/7 1.5 m (orange).

5th percentile (DSM P_5) samples lower sub-canopy heights, roads, and ground gaps between trees and buildings. The median elevation (DSM P_{50}) is less sensitive to vertical outliers and step edges than the arithmetic mean, whereas the 95th percentile (DSM P_{95}) captures the tops of building roofs, ridgelines, and tall tree crowns.

Additionally, the DSM suite includes the local elevation standard deviation (DSM σ_z), defined as the standard deviation of the same unmasked 2.5 m sub-cells inside each $15\,\mathrm{m} \times 15\,\mathrm{m}$ cell. This layer provides a direct measure of sub-cell surface roughness, canopy height variability, and urban structural complexity.

2.1.2 Digital terrain model (DTM) layer

Alongside the DSM layers, the digital terrain model (DTM, in m) provides bare-earth ground elevation on the same 15 m grid, representing the underlying terrain with above-ground features (vegetation and buildings) removed. Table 1 summarizes the six layers as they are distributed.

2.1.3 Geodetic reference frames and data distribution

The dataset is partitioned into 13 485 tiles indexed on an integer $1^\circ \times 1^\circ$ latitude–longitude grid using the naming convention `w[m]XXs[m]YY`, where `w` and `s` denote the west longitude and south latitude edges of the tile and `m` indicates a negative

Table 1. GEM-15 data records. All layers share the $15\,\mathrm{m} \times 15\,\mathrm{m}$ UTM grid of their $1^\circ \times 1^\circ$ tile (Sect. 2.1.3) and are referenced orthometrically to the EGM96 geoid. Band identifiers are those of the Cloud-Optimized GeoTIFF (COG) tiles.

Layer	Band identifier	Unit	Data type	Description
DSM	`dsm`	m	`Float32`	Block-mean surface elevation of the unmasked 2.5 m sub-cells (Sect. 2.1.1)
DSM P_5	`dsm_percentile_5`	m	`Float32`	5th percentile of the sub-cell elevations (ground gaps, lower canopy)
DSM P_{50}	`dsm_percentile_50`	m	`Float32`	Median sub-cell elevation
DSM P_{95}	`dsm_percentile_95`	m	`Float32`	95th percentile of the sub-cell elevations (roof ridges, emergent crowns)
DSM σ_z	`dsm_std`	m	`Float32`	Standard deviation of the sub-cell elevations (surface roughness)
DTM	`dtm`	m	`Float32`	Bare-earth terrain elevation, aggregated from the 1 m DTM with DTM $\leq$ DSM enforced (Sect. 3.1.1)

Cells removed by the quality masks of Sect. 3.1.2 are masked in all six bands.

coordinate (e.g., `wm72s42` for $[-72^\circ, -71^\circ] \times [+42^\circ, +43^\circ]$ and `w15sm35` for $[+15^\circ, +16^\circ] \times [-35^\circ, -34^\circ]$). Rather than using an angular geographic grid, each $1^\circ \times 1^\circ$ tile is projected into its local WGS 84 Universal Transverse Mercator (UTM) zone at an exact $15\,\mathrm{m} \times 15\,\mathrm{m}$ pixel spacing with the grid aligned to the UTM zone origin. Because standard 6°-wide UTM zones have boundaries at integer multiples of 6° longitude, every $1^\circ \times 1^\circ$ cell falls within a single UTM zone without crossing a zone boundary; each tile stores the rectangular $15\,\mathrm{m}$ UTM grid enclosing that $1^\circ \times 1^\circ$ box. Vertical elevations are stored in meters referenced orthometrically to the Earth Gravitational Model 1996 (EGM96) geoid. The dataset is distributed as a Google Earth Engine (Gorelick et al., 2017) ImageCollection, in which each tile asset preserves its native $15\,\mathrm{m}$ UTM projection and can be mosaicked or reprojected on the fly; as $1^\circ \times 1^\circ$ UTM Cloud-Optimized GeoTIFF (COG) tiles on Google Cloud Storage with a retention policy set.

To comply with the Government of India's National Geospatial Policy and remote sensing regulations (Department of Science and Technology, Government of India, 2021, 2022), high-resolution geospatial data across India must meet absolute vertical accuracy limits of $> 3\,\mathrm{m}$. In accordance with these guidelines, vertical offsets have been incorporated into the 15 m GEM-15 DSM and DTM datasets covering India, tapering off outside India over tens of kilometers (see Sects. 3.2.1–3.2.3).

2.2 Source imagery

GEM-15 is generated from a global archive of multi-view and multi-temporal optical stereo satellite imagery collected through 2024 by commercial Airbus and Maxar constellations, spanning native ground sample distances (GSDs) from 0.3 to 1.5 m (Fig. 2). The primary source is the Airbus Pléiades Neo constellation (0.30 m panchromatic and 1.2 m multispectral GSD), whose imagery was acquired from 2022 through 2024 and which serves as the dominant sensor across 63.2 % of mapped

Table 2. Summary of openly available global elevation models.

Model	Grid spacing	Source acquisition	Spatial extent	Provided layers	Sensing modality	Vertical datum	Summary and primary references
SRTM v3	$1''$ ($\approx 30\,\mathrm{m}$)	Feb 2000	$60°\mathrm{N}$–$56°\mathrm{S}$	DSM	Single-pass C-band InSAR ($5.6\,\mathrm{cm}$, $5.3\,\mathrm{GHz}$)	EGM96	Space Shuttle Endeavour 11-day radar mission; void-filled with ASTER GDEM2 (Farr et al., 2007)
NASADEM	$1''$ ($\approx 30\,\mathrm{m}$)	Feb 2000 (released 2020)	$60°\mathrm{N}$–$56°\mathrm{S}$	DSM	Reprocessed C-band InSAR + ICESat GLAS	EGM96	Reprocessed SRTM telemetry with improved phase unwrapping, ICESat GCP calibration, and GDEM v3 / AW3D30 void fill (Crippen et al., 2016; NASA JPL, 2020)
ALOS AW3D30	$1''$ ($\approx 30\,\mathrm{m}$)	2006–2011	$82°\mathrm{N}$–$82°\mathrm{S}$	DSM	Optical tri-stereo (ALOS PRISM, $2.5\,\mathrm{m}$ GSD)	EGM96	Downsampled from the $5\,\mathrm{m}$ AW3D DSM reconstructed from nadir, forward, and backward PRISM views (Takaku et al., 2014; Tadono et al., 2015)
Copernicus GLO-30	$1''$ ($\approx 30\,\mathrm{m}$)	2011–2015	$90°\mathrm{N}$–$90°\mathrm{S}$	DSM	Bistatic X-band InSAR (TanDEM-X, $3.1\,\mathrm{cm}$, $9.65\,\mathrm{GHz}$)	EGM2008	Derived from edited $12\,\mathrm{m}$ WorldDEM with water flattening, coastline editing, and artifact removal (Krieger et al., 2007; Rizzoli et al., 2017; European Space Agency, 2022)
FABDEM	$1''$ ($\approx 30\,\mathrm{m}$)	2011–2015 (GLO-30 base)	$80°\mathrm{N}$–$60°\mathrm{S}$	DTM	Random-forest post-processing of GLO-30	EGM2008	Subtracts GEDI- and ICESat-2-estimated forest canopy and building heights from the $30\,\mathrm{m}$ GLO-30 DSM (Hawker et al., 2022)
GEM-15 (this work)	$15\,\mathrm{m}$	Through 2024	$84°\mathrm{N}$–$61°\mathrm{S}$ †	DSM, P_5, P_{50}, P_{95}, DSM σ_z, DTM	Multi-view optical stereo (0.3–$1.5\,\mathrm{m}$ GSD)	EGM96	Aggregated from quality-screened $0.5\,\mathrm{m}$ stereo+ML DSMs and $1.0\,\mathrm{m}$ CNN bare-earth DTMs on a uniform $15\,\mathrm{m}$ UTM grid

†Excludes Russia, China, Mongolia, and Greenland.

tiles. Another 24.4 % of tiles draw primarily from additional sub-meter Airbus and Maxar satellites (WorldView-3 (0.31 m panchromatic, 1.24 m multispectral), WorldView-4 (0.31 m), GeoEye-1 (0.41 m), WorldView-2 (0.46 m), and Pléiades 1A/1B (0.50 m)) where Pléiades Neo data are unavailable. The remaining 12.4 % of tiles are covered by wide-swath stereo imagery from SPOT-6 and SPOT-7 (1.5 m panchromatic GSD), mainly in sparsely populated boreal, desert, and remote rural regions where sub-meter stereo acquisitions are sparse.

2.3 Baseline DEMs

To benchmark the performance of GEM-15, we compare it against three open 30 m global DSMs as well as the 30 m FABDEM, which is a bare-earth DTM. We summarize the openly available global DEMs in Table 2.

2.3.1 Copernicus GLO-30

The Copernicus GLO-30 is a global DSM derived from the TanDEM-X mission data, which employed bi-static X-band (9.65 GHz, 3.1 cm wavelength) SAR interferometry from two satellites flying in close formation (Rizzoli et al., 2017; Krieger et al., 2007). The radar data were acquired between 2011 and 2015, and the product underwent extensive post-processing including water body flattening, coastline editing, and artifact removal (European Space Agency, 2022). GLO-30 is distributed on a 1 arc-second grid ($\sim$30 m at the equator, with the longitude spacing increasing poleward) and is freely available; it is derived from 0.4 arc-second ($\sim$12 m) TanDEM-X data and has an effective spatial resolution of about 30 m. Global validation against ICESat/GLAS yielded a bare-ground bias below 0.05 m and an RMSE below 0.55 m (Simard et al., 2024), the lowest

among the open global 30 m DSMs. As an X-band radar product, GLO-30 exhibits positive elevation biases over forested areas due to limited canopy penetration, with the bias varying approximately linearly with canopy height (Simard et al., 2024).

2.3.2 ALOS AW3D30

The ALOS World 3D 30 m model (AW3D30) is a global DSM generated by the Japan Aerospace Exploration Agency (JAXA) from optical stereo imagery acquired by the Panchromatic Remote-sensing Instrument for Stereo Mapping (PRISM) aboard the Advanced Land Observing Satellite (ALOS) between 2006 and 2011 (Takaku et al., 2014; Tadono et al., 2015). PRISM acquires imagery from three viewing directions (nadir, forward, and backward), enabling stereoscopic height reconstruction. AW3D30 is provided on a 1 arc-second grid ($\sim$30 m) and is freely available; it is average-downsampled from the 5 m AW3D DSM (itself reconstructed from 2.5 m PRISM panchromatic stereo), giving an effective spatial resolution of ~ 30 m. As an optical stereo product, it measures the top of the visible surface and is affected by cloud cover and low-contrast conditions, resulting in higher noise levels and occasional artifacts compared to radar-derived products. Its nominal vertical accuracy is approximately 5 m RMSE (Takaku et al., 2014; Tadono et al., 2015).

2.3.3 NASADEM

NASADEM is the latest reprocessing of the Shuttle Radar Topography Mission (SRTM) data, released in 2020 (Crippen et al., 2016; NASA JPL, 2020). SRTM acquired single-pass C-band (5.3 GHz, 5.6 cm wavelength) InSAR data during an 11-day mission aboard the Space Shuttle Endeavour in February 2000, covering land surfaces between 56° S and 60° N (Farr et al., 2007). Key improvements in NASADEM over earlier SRTM releases include updated interferometric phase unwrapping and height-ripple error corrections (HREC) calibration using ICESat/GLAS ground control points (Schutz et al., 2005; Zwally et al., 2002), reducing the bare-ground RMSE from approximately 2.5 m to 1.5 m (Simard et al., 2024). NASADEM is provided on a 1 arc-second grid ($\sim$30 m at the equator). Remaining voids are filled using ASTER GDEM v3 and AW3D30 data (Crippen et al., 2016; NASA JPL, 2020).

2.3.4 FABDEM

For a bare-earth DTM baseline, we include FABDEM (Hawker et al., 2022), a 30 m global DTM generated by applying random-forest machine learning to subtract estimated forest canopy and building heights from the 30 m Copernicus GLO-30 DSM.

2.4 Validation reference data

2.4.1 GEDI spaceborne lidar

We use spaceborne lidar observations from the Global Ecosystem Dynamics Investigation (GEDI) Level 2A (version 2) product (Dubayah et al., 2020), which provides ground and canopy height retrievals across 25 m diameter footprints between 51.6° N and 51.6° S from the International Space Station. While individual shots are affected by horizontal geolocation uncertainty

Table 3. Airborne (ALS) and drone (UAV) lidar datasets used for validation, ordered by acquisition date.

Country / Region	Dataset / Source	Ref. Date	Native Res.	Evaluated Extent	Geographic / Ecoclimatic Coverage
Mozambique	NASA CMS Zambezi (ORNL DAAC)	May 2014	$1.0\,\mathrm{m}$	8.8×10^6 px	Zambezi delta coastal mangroves and miombo woodland
Indonesia†	NASA CMS Kalimantan (ORNL DAAC)	Oct 2014	$1.0\,\mathrm{m}$	1.9×10^6 px	Central Kalimantan peat swamp and lowland rainforest
Brazil†	NASA Sustainable Landscapes (ORNL)	2012–2018	$1.0\,\mathrm{m}$	1.1×10^6 px	Amazonian and Cerrado dense forest research transects
Spain	CNIG / IGN PNOA lidar	2018	$1.0\,\mathrm{m}$	16.5×10^6 px	Peninsular Mediterranean forest and semi-arid terrain
US Tropical	NASA CMS / USGS 3DEP (FL & PR)	Mar 2020	$1.0\,\mathrm{m}$	1.4×10^6 px	Subtropical mangrove (Everglades) and insular forest
United Kingdom	Environment Agency National lidar	2020–2022	$1.0\,\mathrm{m}$	9.1×10^6 px	England agricultural, riparian, and built terrain
Canada	NRCan CanElevation / HRDEM	2020–2023	$1.0\,\mathrm{m}$	4.8×10^6 px	Boreal shield forest and temperate montane transects
Global (urban)‡	Tech Mahindra Global Drone-lidar	Jun 2023	0.25–$0.3\,\mathrm{m}$	375×10^3 px	64 urban and peri-urban sites across 10 countries
Global (trees)	3D Trees Research Drone-lidar	2023–2025	0.1–$0.5\,\mathrm{m}$	12×10^3 px	High-density multi-site forest and orchard canopy plots
United States	NSF NEON Airborne Platform	2022–2025	$1.0\,\mathrm{m}$	43.4×10^6 px	Continental observatories across 20 ecoclimatic domains
New Zealand	LINZ National lidar (OpenTopography)	2024–2025	$1.0\,\mathrm{m}$	9.5×10^6 px	High-relief temperate terrain and native evergreen forest
India‡	Tech Mahindra India Drone-lidar	Aug–Oct 2024	0.25–$0.3\,\mathrm{m}$	522×10^3 px	15 tier-1/tier-2 cities across 5 Indian states (urban/peri-urban)

Evaluated extents correspond to the total number of valid $15\,\mathrm{m} \times 15\,\mathrm{m}$ cells across the intersected multi-model evaluation masks plotted in Figs. 6 and 10 and reported in Tables E1–E2. Date ranges denote multi-year tile acquisitions. †Closed-canopy tropical rainforest campaigns, included in all accuracy statistics but excluded from the temporal trend analysis (Sect. 3.2.2). ‡Proprietary commissioned UAV validation datasets used under commercial license (Appendix D).

($\approx 10\,\mathrm{m}$; Beck et al. 2021; Tang et al. 2023) and waveform broadening over steep terrain (Liu et al., 2021), GEDI's broad latitudinal sampling offers a consistent global reference for evaluating continental-scale vertical accuracy (see Sect. 3.2.1 for quality filtering and processing details).

2.4.2 National airborne and drone lidar benchmarks

To evaluate fine-scale topographic accuracy, we compiled 12 high-resolution (0.1–1.0 m native resolution) airborne laser scanning (ALS) and uncrewed aerial vehicle (UAV) drone lidar datasets distributed across six continents (Table 3). Nine of these datasets come from national and regional airborne campaigns across the continental United States (NSF NEON; Kampe et al. 2010; NEON 2026), the tropical United States (Florida and Puerto Rico; Cook et al. 2013; Leitold et al. 2021), Canada (Natural Resources Canada, 2025), New Zealand (Land Information New Zealand, 2025), the United Kingdom (Environment Agency, 2022), Spain (Instituto Geográfico Nacional, 2024), Brazil (dos Santos et al., 2019), Indonesia (Melendy et al., 2017), and Mozambique (Fatoyinbo and Trettin, 2017). We combine these airborne benchmarks with three centimeter-scale UAV lidar benchmarks: two commercially commissioned drone campaigns collected by Tech Mahindra across 15 cities in India (August–October 2024) and across 64 urban and peri-urban sites in 10 countries globally (June 2023; see Appendix D for site coverage, acquisition specifications, and licensing details), alongside open multi-region forest plots from the 3D Trees project (Gerberding et al., 2026; Puliti et al., 2023).

2.4.3 GNSS CORS reference stations

Continuously Operating Reference Stations (CORS) (Snay and Soler, 2008; Johnston et al., 2017) provide permanent GNSS antenna positions with millimeter-level precision, serving as an independent geodetic elevation benchmark worldwide. We

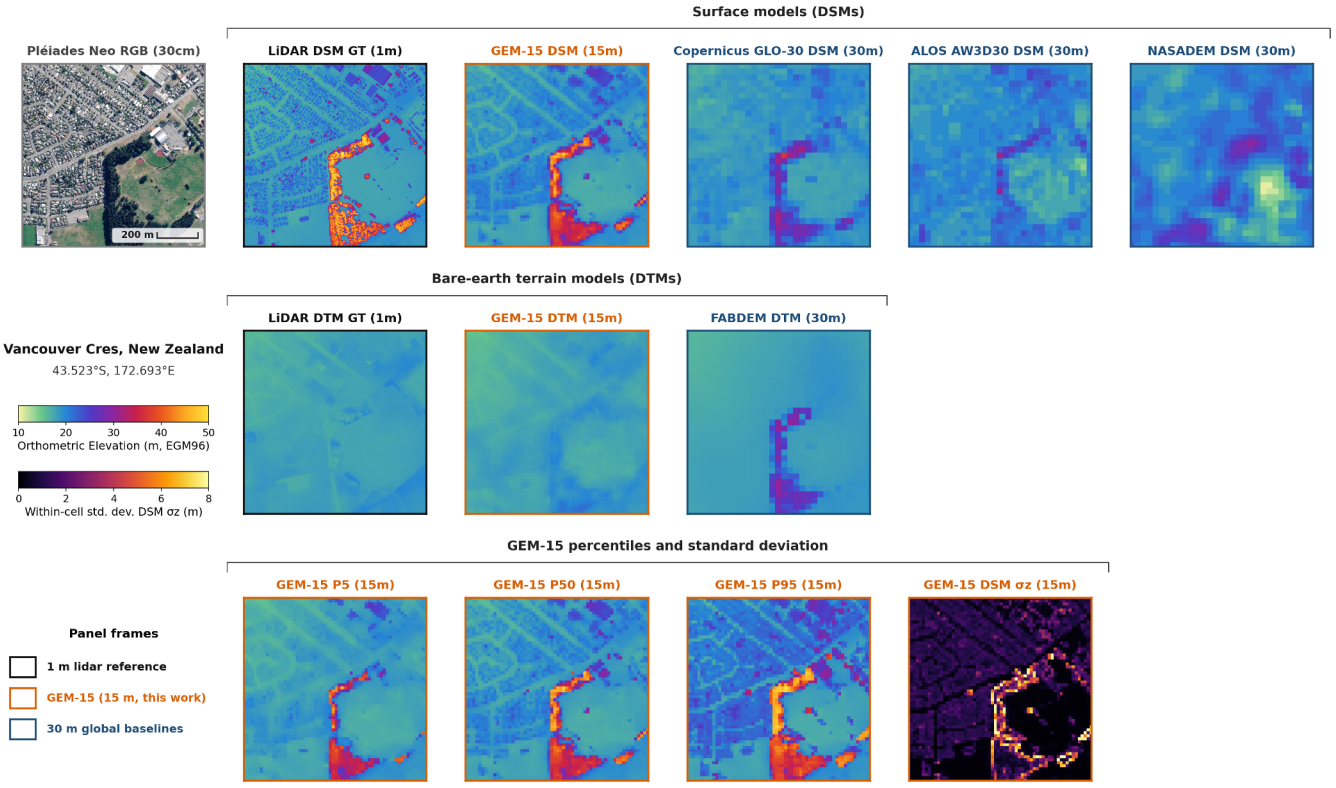


Figure 3. Elevation products over Vancouver Crescent, Christchurch, New Zealand ($43.523^{\circ}\mathrm{S}, 172.693^{\circ}\mathrm{E}$). Rows compare, within each product family, the 1 m airborne lidar reference (black frames) with GEM-15 (15 m; orange frames) and the 30 m baselines (grey frames): surface models (top), bare-earth terrain models (middle), and the GEM-15 sub-cell percentile and standard deviation layers (bottom). The left column shows the Pléiades Neo 30 cm imagery and the colorbars for elevation and within-cell standard deviation.

use 2025-epoch station coordinates from 4 071 international GNSS CORS monuments distributed across six continents: North America ($N = 1\,697$), Europe ($N = 1\,238$), Asia ($N = 527$), Oceania ($N = 305$), South America ($N = 228$), and Africa ($N = 76$).

3 Methods and evaluation

This section describes the two-stage pipeline used to generate GEM-15 from sub-meter optical satellite imagery (Sect. 3.1) and the validation framework used to evaluate vertical and structural accuracy (Sect. 3.2). Figure 3 shows the resulting layers alongside the 30 m baselines over a residential neighborhood in Christchurch, New Zealand.

3.1 Producing the 15 m elevation models globally

The production pipeline operates in two stages: (1) constructing the native 0.5 m DSMs via deep learning paired with multi-view optical photogrammetry and producing 1.0 m bare-earth DTMs via deep learning (Sect. 3.1.1), and (2) applying automated quality masking followed by statistical block aggregation to generate the final 15 m products (Sect. 3.1.2).

3.1.1 Producing high-resolution sub-meter DSMs and DTMs

To generate native 0.5 m DSMs from overlapping multi-temporal satellite passes, we first pose the satellite imagery by refining the sensor rational polynomial coefficient (RPC) projection models provided with the images (Tao and Hu, 2001; Grodecki and Dial, 2003). Starting from coarse JAXA ALOS AW3D30 terrain data (Takaku et al., 2014; Tadono et al., 2015) as an initial prior, we alternate between estimating a surface heightmap (DSM) and computing geometric shifts on images orthorectified with the current height estimate, progressing iteratively from low ($\sim 15\,\mathrm{m}$) to high ($\sim 0.5\,\mathrm{m}$) resolution. At each iteration and pixel, we test vertical offsets around the current height estimate and select the offset that maximizes multi-view appearance similarity after orthorectification. Coupling the horizontal shift estimation with the heightmap update produces mutually consistent orthorectified images. The intermediate DSM from this alignment step is of moderate quality and is used only for sensor pose correction, not in later stages.

Using the refined sensor poses, we generate the native DSM by combining multi-view stereo (MVS) with machine learning (ML) refinement. First, we compute coarse 1.0 m depth maps from a temporal stack of historical imagery (including Pléiades Neo, WorldView-3, SPOT, and other commercial sensors) using plane-sweep stereo with horizontal planes (Gallup et al., 2007). We then fuse these depth maps into an initial DSM via graph-cut optimization, fitting a smooth heightfield to the dense stereo point cloud (Boykov et al., 2001).

For finer structural detail, we run high-resolution MVS on a subset of optimal stereo pairs per location, selected to balance spatial resolution, acquisition recency, and viewing azimuth coverage while keeping compute costs manageable. Each high-resolution depth map is paired with one selected RGB view at a time; the reference RGB image, the view-aligned initial DSM, and the high-resolution depth map are fed to a Swin transformer encoder based U-Net that estimates metric depth from an off-nadir perspective, similar to Batchu et al. (2024). This model was trained using DSMs derived from proprietary high-resolution aerial stereo imagery as labels, as described in Batchu et al. (2024). These ML-derived depth maps are then fused at 12.5 cm resolution via graph-cut optimization (Boykov et al., 2001) and downsampled to 0.5 m to produce the final native DSM.

To recover bare-earth elevation, we estimate the DTM at 1.0 m spatial resolution using a seven-stage, multi-scale residual U-Net (Ronneberger et al., 2015; He et al., 2016). Rather than using two-stage cut-and-fill filters that mask out segmented buildings and trees and interpolate across the resulting voids (Sithole and Vosselman, 2004; Zhang et al., 2016), which often leave boundary artifacts around sharp elevation steps, our network operates directly on $1024\,\mathrm{m} \times 1024\,\mathrm{m}$ UTM tiles ($1.0\,\mathrm{m}$ cell size, with $64\,\mathrm{m}$ overlapping margins to prevent seam artifacts). It takes a four-channel input (co-registered RGB and mean-normalized DSM) and predicts the DTM directly. We train and validate the network against 1.0 m airborne lidar bare-earth DTMs from the USGS 3D Elevation Program (3DEP; Stoker and Miller 2022) across the United States. During training, each

3DEP tile is vertically co-registered to the stereo DSM using the median offset over bare-ground pixels (excluding buildings, trees, and water), and the network is trained with a mean-squared error loss. At inference, we enforce physical consistency by clamping the predicted 1.0 m DTM to the DSM (DTM $\leq$ DSM) and apply a Gaussian filter with a $3\,\mathrm{m}$ radius to smooth residual noise beneath large roofs and closed canopies.

None of the DSM or DTM validation benchmarks in Sect. 2.4 were used for training either of the DSM/DTM estimation models. Because 3DEP covers most of the conterminous United States, the US NEON and US Tropical benchmarks may nevertheless overlap spatially with 3DEP collections that entered DTM training. The DTM model, although trained only on US 3DEP data, achieves accuracy on the airborne and drone lidar benchmarks outside the United States that is comparable to its accuracy within the United States (Sect. 4.2), with reduced accuracy beneath dense, closed forest canopies.

Samples of the native 0.5 m DSMs and 1.0 m DTMs are shown in Appendix C (Fig. C1). Because the underlying sub-meter optical stereo imagery and derived native-resolution DSMs and DTMs are covered by commercial satellite licensing agreements that restrict open global redistribution at native resolution, these intermediate high-resolution products remain proprietary.

3.1.2 Downsampling to 15 m DSMs with quality masking

To ensure that stereo-matching errors and atmospheric anomalies are eliminated during spatial downsampling, three filters are applied across the native 0.5 m and 15 m target grids.

First, on the raw 0.5 m pixels, we mask water using an internal water detection model. In mountainous terrain, water classifiers often misclassify dark shadows along sides of mountains as water, causing stereo pipelines to flatten steep slopes. To prevent this, we dilate the water mask by a 9.0 m circular radius and mask all pixels within the buffer which excludes dark mountain slopes. Second, after aggregating to 15 m, we exclude 15 m cells whose DSM elevation differs by more than 50 m from Copernicus GLO-30 ($|\Delta z| > 50\,\mathrm{m}$), removing stereo-matching blunders and clouds. Third, we remove planar artifacts over featureless terrain such as alpine snowfields, flat deserts, and glaciated plateaus, where insufficient optical features cause photogrammetric matching to fail, producing artificial stepped blocks (Shean et al., 2016). We detect these regions at 15 m resolution using the within-cell standard deviation (DSM $\sigma_z < 0.02\,\mathrm{m}$ over non-water cells) and apply a 60 m square erosion followed by a 120 m square dilation to mask contiguous flat blocks and their boundaries, removing the square planar artifacts that otherwise appear over snow and ice fields such as in the Swiss Alps (Fig. 4).

We use a two-stage aggregation scheme that balances computational cost at global scale with sub-pixel fidelity. Native 0.5 m DSMs and 1 m DTMs are first bilinearly resampled to an intermediate 2.5 m grid (6×6 sub-cells per 15 m cell), and the unmasked 2.5 m DSM sub-cells are then block-reduced using the arithmetic mean within each $15\,\mathrm{m} \times 15\,\mathrm{m}$ cell (the two-stage scheme agrees with direct $0.5\,\mathrm{m}$ block reduction to within $0.02\,\mathrm{m}$ DRMSE across all six layers; Appendix B). The 5th, 50th, and 95th elevation percentiles (DSM P_5, DSM P_{50}, DSM P_{95}) and local standard deviation (DSM σ_z) are computed simultaneously across the same unmasked 2.5 m sub-cells. The 1 m DTM predictions are aggregated using the median of the unmasked 2.5 m sub-cells and clamped to the 15 m DSM (DTM $\leq$ DSM), after which the 15 m Copernicus GLO-30 and planar-artifact masks are applied across all elevation layers.

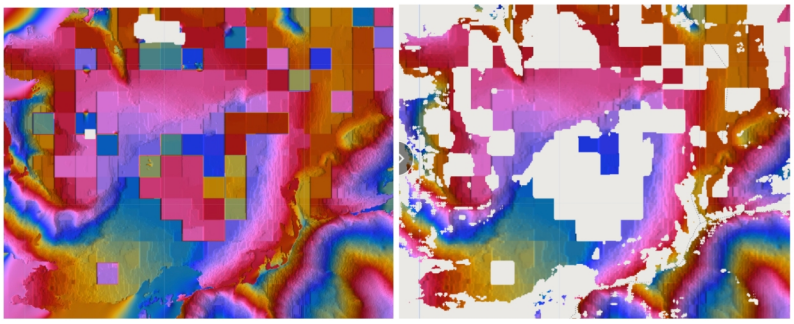


Figure 4. Quality masking over high-relief glaciated terrain in the Swiss Alps, showing the raw pre-filter DSM (left) and the post-filter DSM after low-variance planar artifact and gross outlier ($|\Delta z| > 50\,\mathrm{m}$) masking (right).

Across the global landmass, this quality filtering masks out approximately 2.5 % of cells, with voids concentrated over perennial snowfields, glaciated mountain peaks, and inland water bodies. For hydrological and environmental modeling requiring gap-free terrain, these masked cells can be filled using the Copernicus GLO-30 DEM at some cost to accuracy for those areas.

3.2 Verification and validation

To assess the vertical accuracy of GEM-15, we conduct all airborne and drone lidar evaluations at 15 m resolution. Evaluating at 15 m rather than coarsening to 30 m allows us to compare GEM-15 and the existing global baselines at the highest available grid resolution across all available global products. The resulting metrics therefore describe the accuracy of each product as delivered to a user working on a 15 m grid, and part of the error attributed to the 30 m products on this grid is representation error of their coarser posting rather than sensor error (Sect. 5.1). High-resolution airborne and UAV lidar reference datasets are aggregated to the 15 m grid via block-mean reduction, while the 30 m baseline products (Copernicus GLO-30, ALOS AW3D30, NASADEM, and FABDEM) are bilinearly interpolated to 15 m and vertically aligned to the EGM96 orthometric geoid (Lemoine et al., 1998) (converting Copernicus GLO-30 and FABDEM from EGM2008 (Pavlis et al., 2012) to EGM96 using the geoid undulation difference $N_{\mathrm{EGM2008}} - N_{\mathrm{EGM96}}$). The GEDI evaluation, however, is conducted at GEDI's native 25 m resolution, with GEM-15 and all baseline products resampled to 25 m because each GEDI shot integrates returns across a 25 m footprint diameter.

Our validation framework randomly samples non-overlapping $1.5\,\mathrm{km} \times 1.5\,\mathrm{km}$ evaluation tiles (100×100 cells at 15 m resolution) across each benchmark region, restricting evaluation to cells that are valid across the reference dataset and all compared baseline products. For GEDI evaluation in particular, we stratify sampling evenly across MODIS MCD12Q1 land-cover classes (Friedl and Sulla-Menashe, 2019; Sulla-Menashe et al., 2019) to ensure an even representation of validation cells. To prevent sparsely populated tiles from carrying the same weight as fully populated ones, we pool valid cells across all K evaluation tiles rather than averaging per-tile RMSE or bias. Within each tile $k \in \{1, \ldots, K\}$ containing M_k valid cells, we first

compute the local vertical bias to account for localized datum offsets:

$$\text{Bias}_k = \frac{1}{M_k} \sum_{i=1}^{M_k} \left(z_{\text{DEM},k,i} - z_{\text{ref},k,i} \right), \tag{1}$$

where $z_{\text{DEM},k,i}$ and $z_{\text{ref},k,i}$ denote the evaluated elevation model and the co-registered reference elevation at cell i in tile k, respectively. Letting $N = \sum_{k=1}^{K} M_k$ denote the total number of valid evaluation cells across a benchmark, we compute the global mean bias, direct root-mean-square error (RMSE), tile-debiased root-mean-square error (DRMSE), and tile-debiased normalized median absolute deviation (NMAD) across all N pooled cells:

$$\text{Bias} = \frac{1}{N} \sum_{k=1}^{K} \sum_{i=1}^{M_k} (z_{\text{DEM},k,i} - z_{\text{ref},k,i}) = \frac{1}{N} \sum_{k=1}^{K} M_k \, \text{Bias}_k, \tag{2}$$

$$\text{RMSE} = \sqrt{\frac{1}{N} \sum_{k=1}^{K} \sum_{i=1}^{M_k} (z_{\text{DEM},k,i} - z_{\text{ref},k,i})^2}, \tag{3}$$

$$\begin{aligned} \text{DRMSE} &= \sqrt{\frac{1}{N} \sum_{k=1}^{K} \sum_{i=1}^{M_k} \left((z_{\text{DEM},k,i} - z_{\text{ref},k,i}) - \text{Bias}_k \right)^2} \\ &= \sqrt{\frac{1}{N} \sum_{k=1}^{K} M_k \left(\text{RMSE}_k^2 - \text{Bias}_k^2 \right)}, \end{aligned} \tag{4}$$

$$\text{NMAD} = 1.4826 \times \text{median}_{k,i} \left(|\Delta z_{k,i} - \text{median}_j(\Delta z_{k,j})| \right), \tag{5}$$

where $\text{RMSE}_k = \sqrt{\frac{1}{M_k} \sum_{i=1}^{M_k} (z_{\text{DEM},k,i} - z_{\text{ref},k,i})^2}$ is the direct RMSE within tile k, $\Delta z_{k,i} = z_{\text{DEM},k,i} - z_{\text{ref},k,i}$, $\text{median}_j(\Delta z_{k,j})$ is the median vertical residual within tile k ($j \in \{1, \ldots, M_k\}$), and $\text{median}_{k,i}$ is evaluated across all N valid cells pooled over $k \in \{1, \ldots, K\}$ and $i \in \{1, \ldots, M_k\}$ (using $1\,\text{cm}$ error histograms).

We use tile-debiased RMSE (DRMSE) as our primary metric because it isolates local geometric accuracy from broad-scale datum offsets. Alongside DRMSE, we report NMAD (Höhle and Höhle, 2009) as an outlier-resistant measure of vertical dispersion and mean bias (μ) to quantify systematic vertical shifts. To assess performance across different surface types, we stratify all valid evaluation cells along two dimensions: (1) surface height above ground, separating bare-ground and low-vegetation cells ($\leq 5\,\text{m}$ reference height above ground) from above-ground structures ($> 5\,\text{m}$, such as forest canopies and buildings); and (2) topographic relief, separating flat terrain (slope $< 10°$) from steep terrain (slope $\geq 10°$). Within each stratum, Bias_k and the tile median are recomputed from the cells of that stratum in tile k, i.e., each stratum is debiased independently. Because the overall statistics retain the vertical offset between strata within a tile (e.g., between canopy and bare ground), the overall DRMSE can exceed the DRMSE of both constituent strata. In addition, we evaluate the GEM-15 percentile layers (P_5, P_{50}, P_{95}) and within-cell standard deviation (DSM σ_z) against the exact 15 m block statistics computed from the native airborne and drone lidar DSMs. Lastly, we benchmark the 15 m GEM-15 DTM and the 30 m FABDEM product against the lidar DTMs.

3.2.1 Global verification using GEDI spaceborne lidar

For global verification against GEDI Level 2A waveforms, we filter footprints using standard quality and ranging flags (Beck et al., 2021) (quality_flag == 1, degrade_flag == 0, elevation_bias_flag == 0, and beam sensitivity > 0.90), restrict observations to nighttime passes (solar_elevation < 0) to minimize solar background noise, and exclude atmospheric cloud reflections by filtering footprints where the surface elev_lowestmode is $> 100\,\mathrm{m}$ from SRTM. Reference top-of-surface (DSM) elevations are extracted from the highest detected return (elev_highestreturn), while bare-earth ground (DTM) elevations are taken from the lowest waveform mode (elev_lowestmode) and converted from the WGS 84 ellipsoid to the EGM96 geoid. Because laser waveforms do not reliably reach true ground beneath dense canopies or buildings, we mask out ESA WorldCover v200 (Zanaga et al., 2022) tree-cover, built-up, and permanent-water classes specifically during DTM evaluation, while retaining all land-cover classes for DSM evaluation. To align with contemporary surface conditions, we sample 2 205 evaluation tiles (159×10^3 valid footprints) from 2025 GEDI monthly tracks stratified across MODIS MCD12Q1 land-cover classes, excluding tiles over India due to the regulatory vertical offset described in Sect. 2.1.3.

3.2.2 Validation against airborne and drone lidar

For the 12 ALS and UAV lidar benchmarks (Table 3), we aggregate the native 0.1–$1.0\,\mathrm{m}$ DSM and DTM rasters to the 15 m evaluation grid to generate reference layers for the mean DSM, bare-earth DTM, sub-cell percentiles (P_5, P_{50}, P_{95}), and within-cell standard deviation (DSM σ_z). To align the national airborne benchmarks with the EGM96 vertical datum of GEM-15, the reference orthometric heights (NAVD88 in the US, CGVD2013 in Canada, ODN in the UK, NZVD2016 in New Zealand, EGM08-REDNAP in Spain, and local datums in Brazil, Indonesia, and Mozambique) are converted to EGM96 using national geoid grids where available (OSGM15 in the UK, CGVD2013 in Canada, REDNAP in Spain, and NZVD2016 in New Zealand) and by treating the local datum as EGM2008, i.e., applying $N_{\mathrm{EGM2008}} - N_{\mathrm{EGM96}}$, for the remaining benchmarks (US, Brazil, Indonesia, and Mozambique). The tile-debiased DRMSE and NMAD are unaffected by this approximation, whereas the pooled mean biases of these campaigns include any residual offset between the local datum and EGM2008. Across the three UAV campaigns (3D Trees, Global Drone, and India Drone), we report only tile-debiased metrics (DRMSE and NMAD) and omit mean vertical bias (μ) and direct RMSE, as the absolute heights of the drone benchmarks depend on local survey georeferencing (Appendix D) and tile-level debiasing accounts for the regulatory vertical offset on the India Drone benchmark (Sect. 2.1.3).

Comparing airborne campaigns acquired between 2012 and 2025 also requires accounting for physical landscape changes over the time gap $|\Delta t| = |t_{\mathrm{DEM}} - t_{\mathrm{ref}}|$ between satellite observation and reference flight. Older ALS campaigns such as the 2014 Mozambique survey were flown within the TanDEM-X acquisition window for Copernicus GLO-30 (2011–2015) but precede the primary 2022–2024 Pléiades Neo imagery used in GEM-15 by 8–10 years, a period over which land-use change alters the DSMs. We therefore relate the relative DRMSE improvement of GEM-15 over GLO-30 to the reference survey date (using the tile-weighted mean acquisition date for multi-year tile acquisitions), quantified by an ordinary least-squares fit and a Spearman rank correlation. The two closed-canopy tropical rainforest campaigns (Brazil and Indonesia) are reported in all accuracy statistics but excluded from this trend analysis, because their errors are dominated by canopy structure rather than

temporal change (Sect. 4.3). To separate the temporal lag from regional differences across campaigns, we complement the multi-campaign comparison with a longitudinal analysis across fixed cohorts of US NEON sites repeatedly surveyed between 2016 and 2025 (Sect. 4.1.1).

3.2.3 GNSS CORS reference stations analysis

Following earlier GNSS-based assessments of global DEMs (Wessel et al., 2018), we evaluate against the 2025-epoch geodetic coordinates of 4071 active stations worldwide. Because regional GNSS networks use varying antenna mounting configurations (such as ground pillars versus building rooftops) and local vertical datum conventions, we do not apply the tile-level debiasing used for the airborne benchmarks (Eq. 1). Instead, for each elevation model we compute the mean vertical bias across the evaluated station set (across all 4071 stations for the pooled global metric, and across the stations within each continent for the continent-stratified analysis) and subtract it from the corresponding station residuals before computing the debiased vertical RMSE (DRMSE). Because neither a global nor a continental offset removes the country-specific regulatory vertical offset applied only over India (Sect. 2.1.3), residuals at Indian stations make the GEM-15 CORS statistics for Asia and the global network conservative. Station ellipsoidal heights are converted to EGM96 orthometric heights using the EGM96 geoid model, and each DEM is sampled at the station location by bilinear interpolation. While denser national and regional GNSS networks exist in several countries, many are not openly accessible; we therefore restrict our evaluation to the publicly available international GNSS CORS network here.

4 Results

Figure 5 illustrates the differences between GEM-15 and the 30 m baselines across three contrasting landscapes. In forested terrain (Site A, Fig. 5A; Schwarzwald, Germany), the GEM-15 DSM and derived heightmap (DSM − DTM) can resolve individual coniferous tree crowns and narrow forest clearings, whereas the 30 m DSMs smooth out canopy boundaries. In urban areas (Site B, Fig. 5B; Barcelona, Spain), GEM-15 resolves the city blocks, interior courtyards, and streets, which merge into mounds in Copernicus GLO-30. At the Kalgoorlie Super Pit mine (Site C, Fig. 5C; Australia), GEM-15 captures the mining benches and haul roads descending more than $115\,\mathrm{m}$ into the pit, whereas GLO-30 rounds off the bench edges and AW3D30 shows high stereo noise. Additional side-by-side comparisons against lidar reference data across all 12 validation benchmarks are provided in Appendix A (Figs. A1, A2, A3, and A4).

In the sections below, we present the quantitative evaluation starting with the primary 15 m DSM across overall accuracy, temporal alignment, height-above-ground strata, slope regimes, and GNSS CORS monuments (Sect. 4.1), followed by the 15 m bare-earth DTM (Sect. 4.2) and the sub-cell vertical percentile and standard deviation layers (Sect. 4.3). This section reports means, ranges, and the largest differences; the complete per-benchmark DRMSE, bias, and NMAD values for every stratum are provided in Appendix E (Tables E1, E2, E3, and E4).

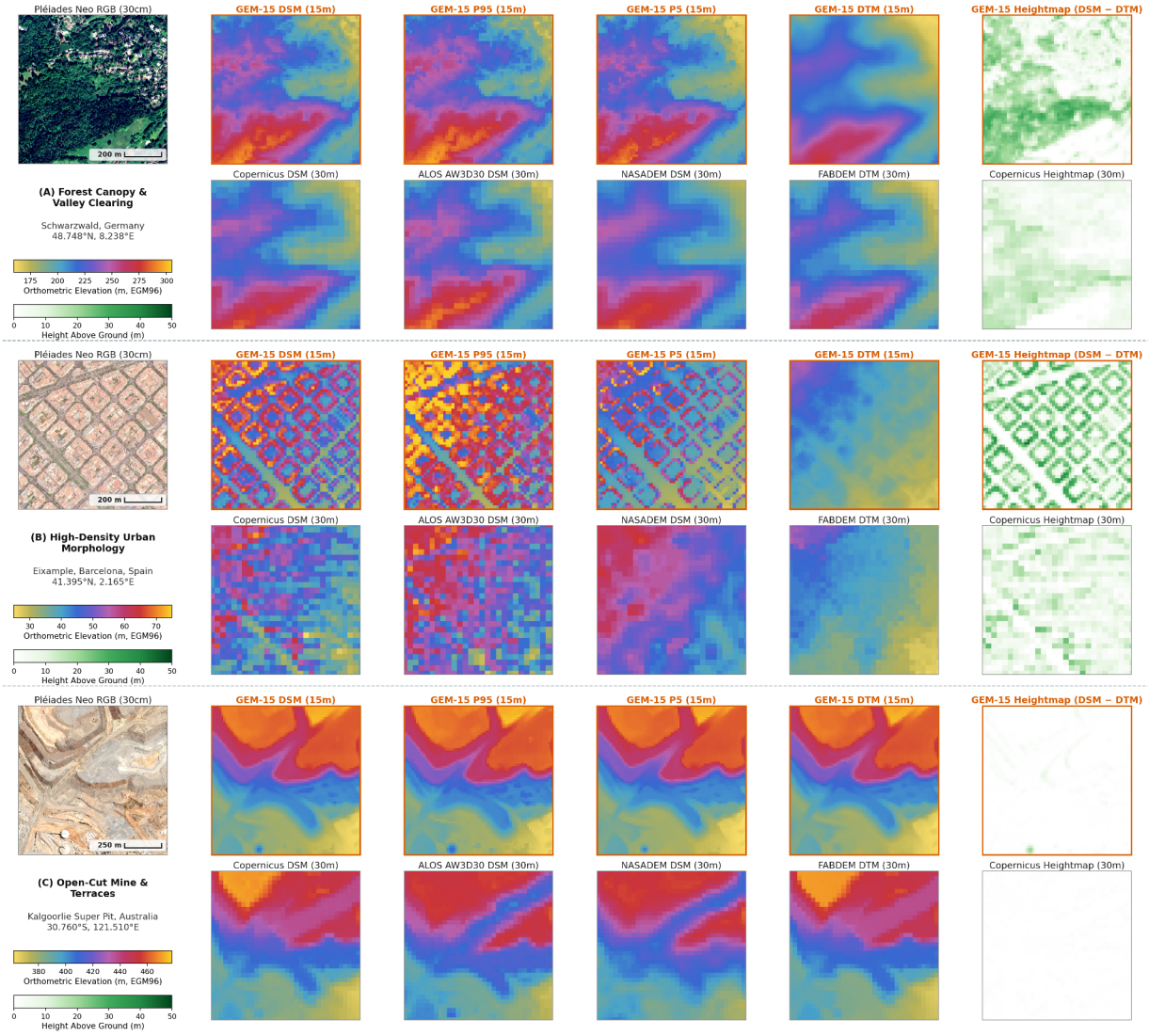


Figure 5. Visual comparison of GEM-15 against 30 m baseline DEMs across three sites: (A) Schwarzwald forest, Germany (48.748°N, 8.238°E), (B) Eixample urban grid, Barcelona, Spain (41.395°N, 2.165°E), and (C) Kalgoorlie Super Pit mine, Australia (30.760°S, 121.510°E). For each site, the top row shows (left to right): Pléiades Neo 30 cm RGB imagery, GEM-15 DSM (15 m), GEM-15 P_{95} (15 m), GEM-15 P_5 (15 m), GEM-15 DTM (15 m), and the GEM-15 heightmap (DSM − DTM); the bottom row shows (left to right): site coordinates and dual colorbars (orthometric elevation in m above the EGM96 geoid and height above ground in m), Copernicus GLO-30 DSM (30 m), ALOS AW3D30 DSM (30 m), NASADEM DSM (30 m), FABDEM DTM (30 m), and the baseline 30 m heightmap (Copernicus GLO-30 DSM − FABDEM DTM). Elevation rasters are normalized to site-specific relief (Turbo colormap), and heightmaps use a common scale from 0 m (white) to 50 m (dark green).

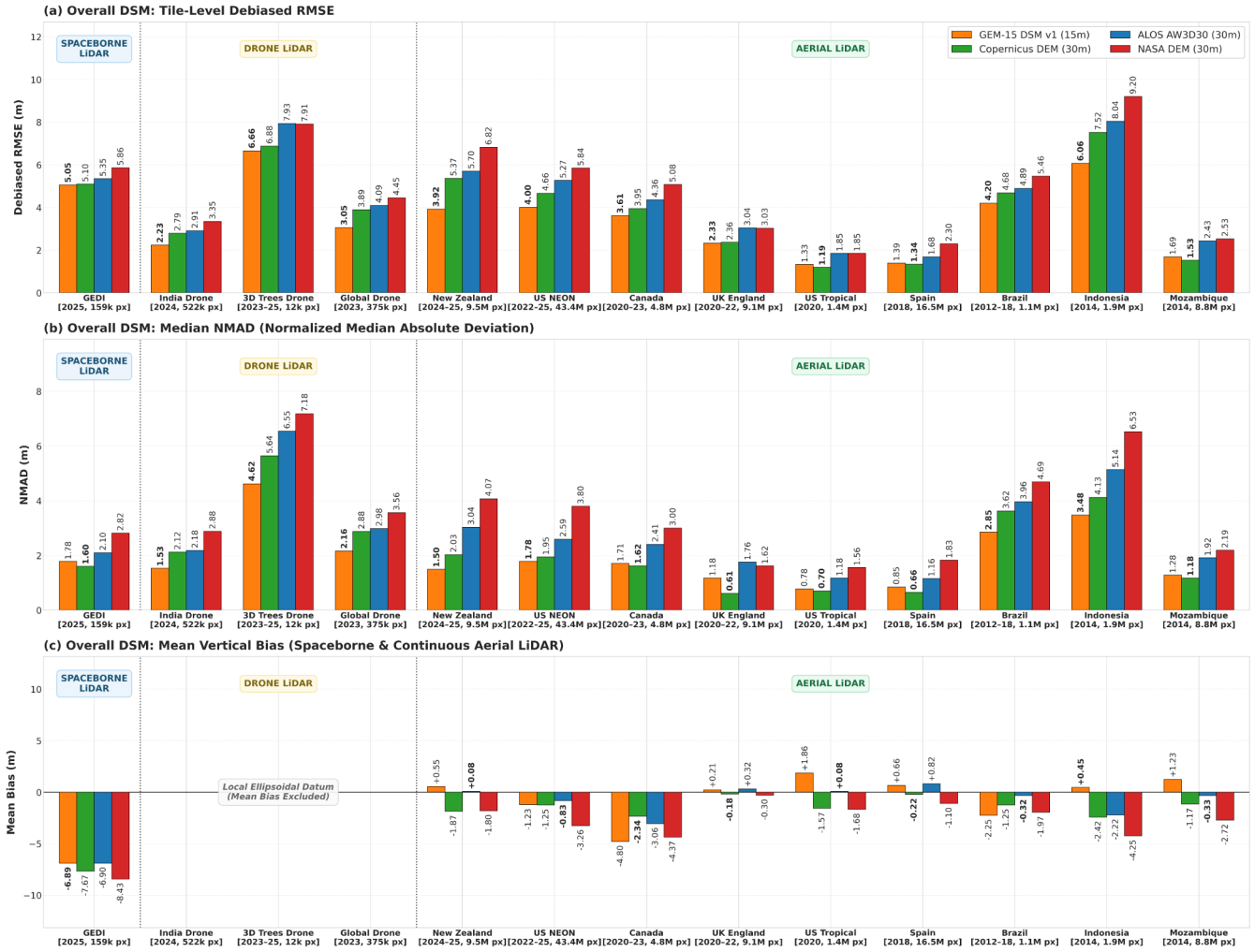


Figure 6. Overall DSM validation metrics for GEM-15, Copernicus GLO-30, ALOS AW3D30, and NASADEM across spaceborne GEDI (2025), three drone lidar benchmarks, and nine national airborne lidar campaigns (acquisition dates in Table 3): (a) tile-level debiased root-mean-square error (DRMSE, in m), (b) normalized median absolute deviation (NMAD, in m), and (c) mean vertical bias ($\mu = \text{DEM} - \text{reference}$, in m; omitted for the three local-datum drone benchmarks).

4.1 Digital surface model (DSM) evaluation

4.1.1 Overall surface accuracy and temporal alignment

On the global GEDI verification benchmark (Fig. 6a,b; Table E1), GEM-15 has the lowest DSM DRMSE of the four models (5.05 m vs. 5.10 m for Copernicus GLO-30) and the second-lowest NMAD (1.78 m vs. 1.60 m for GLO-30); ALOS AW3D30 and NASADEM are higher on both metrics. These values exceed the GEDI-based accuracies usually reported for the 30 m

DEMs because published assessments are typically restricted to open ground on slopes below $5°$ or $10°$ (e.g., Hawker et al., 2022; Simard et al., 2024), where the 25 m footprint and $\approx 10\,\mathrm{m}$ geolocation uncertainty of GEDI introduce little vertical error (Liu et al., 2021), whereas our overall comparison retains all slopes and land-cover classes. Restricting our sample accordingly (slope $< 5°$ and reference height above ground $\leq 5\,\mathrm{m}$; 66×10^3 footprints) gives DRMSE values of 1.21, 0.85, 1.26, and $1.92\,\mathrm{m}$ and NMAD values of 0.63, 0.40, 0.83, and $1.41\,\mathrm{m}$ for GEM-15, GLO-30, AW3D30, and NASADEM, respectively, consistent with the literature and with the same ranking as in the bare ground results in Sect. 4.1.2.

Across the 12 airborne and drone lidar campaigns, the mean campaign DRMSE of GEM-15 is 12.3 % lower than that of Copernicus GLO-30 ($3.37\,\mathrm{m}$ vs. $3.85\,\mathrm{m}$), and 13.7 % lower ($3.69\,\mathrm{m}$ vs. $4.27\,\mathrm{m}$) across the seven benchmarks with acquisition midpoints from 2021 onward (UK, Canada, US NEON, New Zealand, Global Drone, India Drone, and 3D Trees Drone), which overlap the 2022–2024 GEM-15 imagery window. GEM-15 has lower DRMSE than ALOS AW3D30 and NASADEM on every lidar campaign, on GEDI, and at the CORS stations (Sect. 4.1.4). Relative to GLO-30, the per-campaign difference ranges from 11.9 % higher DRMSE (US Tropical) to 26.9 % lower (New Zealand, 2024–2025). GEM-15 is lower on most campaigns, with the largest margins on the most recent or most structured benchmarks (New Zealand, the two commissioned drone benchmarks, the Indonesian rainforest, and US NEON), smaller margins in Brazil and Canada, within a few percent on the UK survey and the 3D Trees forest plots, and higher on three low-relief benchmarks acquired before 2021 (discussed below); per-benchmark DRMSE, NMAD, and bias values are listed in Table E1.

As shown in Fig. 7, the relative DRMSE difference between GEM-15 and Copernicus GLO-30 increases with the acquisition date of the reference lidar survey (Spearman $\rho = 0.87$, $p = 0.001$; linear trend of $+3.44\,\%\,\mathrm{yr}^{-1}$ across the 10 non-rainforest campaigns). Copernicus GLO-30 has the lower DRMSE on the three low-relief benchmarks acquired before 2021 (Mozambique 2014, Spain 2018, and US Tropical 2020), by 0.05–$0.16\,\mathrm{m}$, whereas GEM-15 has the lower DRMSE on every survey with an acquisition midpoint from 2021 onward, by between 1.4 % (UK) and 26.9 % (New Zealand).

To separate this temporal effect from regional differences in relief and land cover across benchmarks, we analyze repeated airborne lidar acquisitions over the US NEON network (Fig. 8). Because NEON does not fly the same set of sites every year, comparing annual averages can conflate temporal change with changing site composition. We therefore track two fixed site cohorts: Series 1 (dashed lines; 14 sites surveyed in 2016, 2017, and 2018) and Series 2 (solid lines; 12 sites surveyed in 2019, 2021, 2023, and 2025). In Series 1, whose surveys predate the GEM-15 imagery, the GEM-15 DRMSE decreases toward the later flights while that of Copernicus GLO-30 increases. In Series 2, the DRMSE of all three 30 m baselines increases over the six years, whereas GEM-15 changes least ($+0.34\,\mathrm{m}$ vs. $+0.61\,\mathrm{m}$ for GLO-30). GEM-15 has the lowest DRMSE in every survey year of both series, and its margin over GLO-30 reaches $1.51\,\mathrm{m}$ against the 2025 flights. The NMAD ordering differs: GLO-30 has the lower NMAD in 2019 and 2021, and GEM-15 is lower from 2023 onward ($1.55\,\mathrm{m}$ vs. $1.66\,\mathrm{m}$ in 2025).

Across the airborne benchmarks, the GEM-15 mean vertical bias (μ; Fig. 6c; Table E1) is within $\pm 1\,\mathrm{m}$ in the UK, Indonesia, New Zealand, and Spain, between 1.2 and $2.3\,\mathrm{m}$ in magnitude in Mozambique, US Tropical, US NEON, and Brazil, and largest in Canada ($-4.80\,\mathrm{m}$). Because DRMSE removes tile-level offsets, these biases do not affect the DRMSE comparisons above.

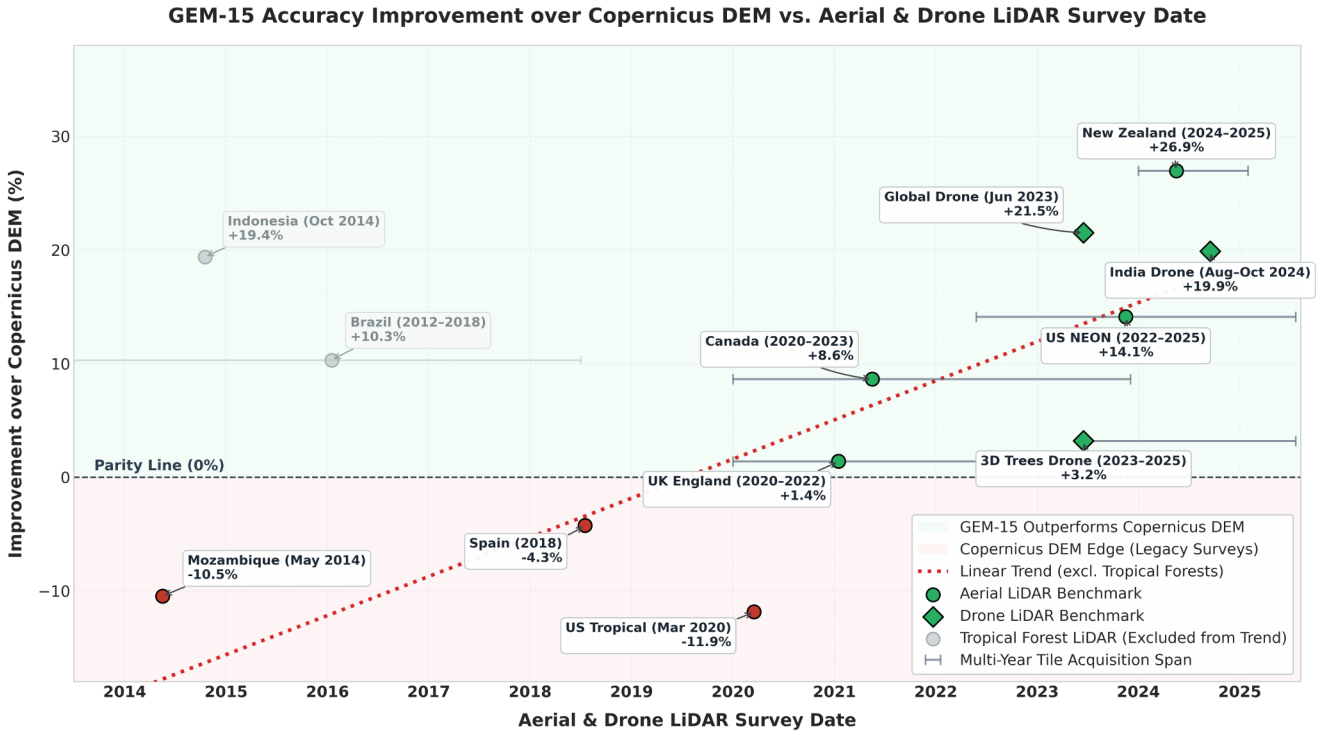


Figure 7. Relative DSM DRMSE improvement (%) of GEM-15 over Copernicus GLO-30 defined as $(\mathrm{DRMSE}_{\mathrm{Copernicus}} - \mathrm{DRMSE}_{\mathrm{GEM\text{-}15}})/\mathrm{DRMSE}_{\mathrm{Copernicus}} \times 100\,\%$, plotted against the reference survey date for all 12 airborne and drone campaigns (2012–2025). Horizontal bars show multi-year tile acquisition spans; points are placed at the tile-weighted mean acquisition date of the evaluated tiles. The linear trend (dotted; $+3.44\,\%\,\mathrm{yr}^{-1}$, $R^2 = 0.67$) and rank correlation (Spearman $\rho = 0.87$, $p = 0.001$; Pearson $r = 0.82$, $p = 0.004$) are computed over 10 campaigns, excluding the two closed-canopy tropical rainforest benchmarks (Brazil and Indonesia; gray), whose errors are dominated by canopy structure rather than temporal change. Including all 12 campaigns gives $\rho = 0.60$ ($p = 0.04$).

4.1.2 Above-ground and bare-ground performance ($> 5\,\mathrm{m}$ vs. $\leq 5\,\mathrm{m}$)

The advantages of sub-meter optical stereo reconstruction are particularly clear over above-ground features ($\mathrm{DSM} - \mathrm{DTM} > 5\,\mathrm{m}$), such as forest canopies and buildings (Table E1). Across this stratum, GEM-15 achieves the lowest DRMSE on most benchmarks, by between 0.5 % (GEDI) and 29.3 % (New Zealand; $4.51\,\mathrm{m}$ vs. $6.38\,\mathrm{m}$), with the larger margins on the closed-canopy rainforest and Global drone benchmarks. GLO-30 has the lower above-ground DRMSE in Canada (by $0.12\,\mathrm{m}$) and in the three older, low-relief benchmarks.

Against GEDI, all four elevation models exhibit a negative mean vertical bias (Fig. 6c, Table E1), because the GEDI DSM reference is the highest detected waveform return. This offset arises from differences in how the sensors sample the canopy profile: whereas GEDI's highest return (elev_highestreturn) records initial laser reflections from the uppermost branch tips within a 25 m footprint, gridded DSMs represent the area-averaged optical surface or radar scattering phase center across a

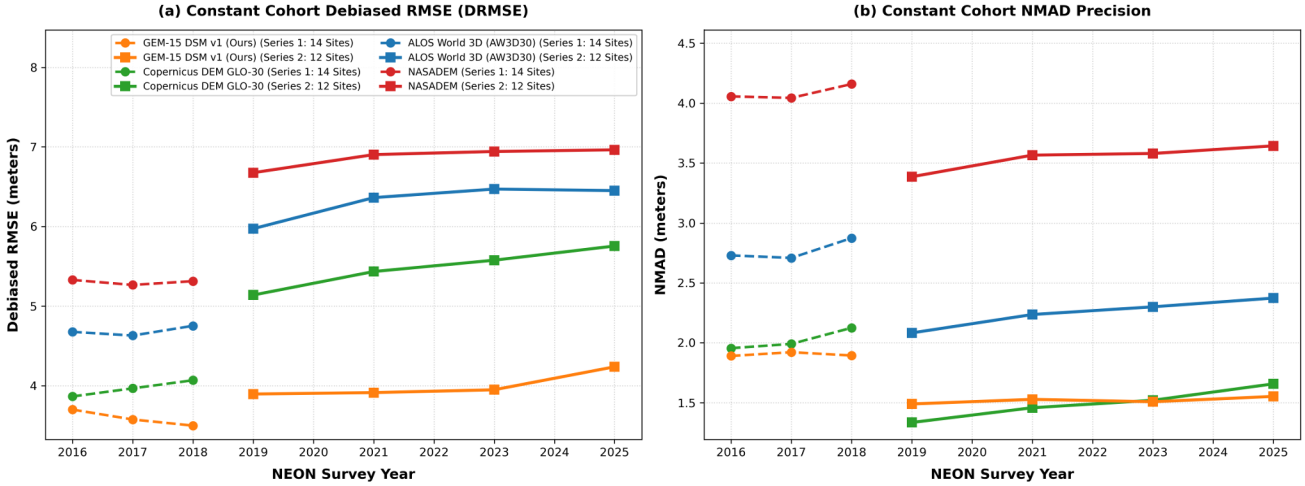


Figure 8. Longitudinal DSM (a) debiased RMSE (DRMSE, in m) and (b) normalized median absolute deviation (NMAD, in m) for GEM-15, Copernicus GLO-30, ALOS AW3D30, and NASADEM across two fixed cohorts of repeatedly surveyed US NEON airborne lidar sites: Series 1 (dashed lines; 14 identical sites, 2016–2018) and Series 2 (solid lines; 12 identical sites, 2019–2025).

15 m or 30 m cell. Because GEM-15 reconstructs canopy geometry at a native 0.5 m resolution before spatial averaging, it preserves upper crown heights and building edges with less smoothing than the 30 m radar baselines, reducing the magnitude of the negative GEDI bias by $0.78\,\mathrm{m}$ relative to Copernicus GLO-30 and by $1.54\,\mathrm{m}$ relative to NASADEM.

Over bare-ground and low-vegetation surfaces (DSM$-$DTM $\leq 5\,\mathrm{m}$; Table E1), the GEM-15 and GLO-30 products are close. Copernicus GLO-30 has the lower DRMSE on most benchmarks, consistent with the low noise of bistatic X-band InSAR over flat, open terrain (Rizzoli et al., 2017), whereas GEM-15 is lower by 12.0–15.3 % on three benchmarks with varied topographic relief (New Zealand, Indonesia, and US NEON) and matches GLO-30 within $0.04\,\mathrm{m}$ in Brazil and Canada.

4.1.3 Flat vs. steep slope performance ($< 10°$ vs. $\geq 10°$)

Stratifying the DSM evaluation by terrain slope (flat, slope $< 10°$, vs. steep, slope $\geq 10°$; Table E1) shows where the finer grid matters most: the margin of GEM-15 over Copernicus GLO-30 is generally wider on steep slopes, where 30 m cells smear valley walls and ridgelines, than on flat terrain, where the two products are closer and GLO-30 is lower on several benchmarks. Errors are generally higher on steeper slopes (with Brazil and Mozambique as exceptions; cf. Hodgson and Bresnahan 2004; Uuemaa et al. 2020), where a single 30 m grid cell spans $\approx 5\,\mathrm{m}$ of vertical change at $10°$ and more than $17\,\mathrm{m}$ at $30°$, and side-looking radar sensors are affected by foreshortening and layover (Rizzoli et al., 2017; Wessel et al., 2018). On flat terrain, GEM-15 has the lower DRMSE on the commissioned benchmarks, New Zealand, US NEON, Canada, and the two rainforest campaigns, by 8–26 %, whereas Copernicus GLO-30 is lower on GEDI, the UK, 3D Trees, and the three low-relief benchmarks (Sect. 4.1.1), by at most $0.16\,\mathrm{m}$. On steep slopes, GEM-15 has the lower DRMSE on most benchmarks, by 2–27 % (largest in New Zealand and the two rainforest campaigns), and its margin is wider than on flat terrain on most benchmarks, although it

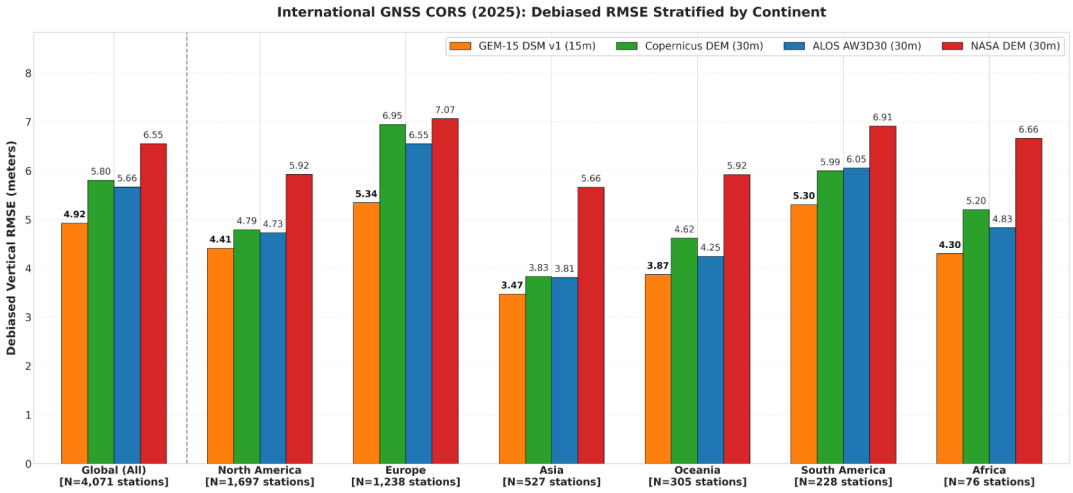


Figure 9. Debiased vertical root-mean-square error (DRMSE, in m) against 4071 international GNSS CORS monuments (2025) for GEM-15, Copernicus GLO-30, ALOS AW3D30, and NASADEM across all pooled stations globally (debiased by the global mean offset) and stratified by continent (debiased by each continent's mean offset).

narrows on Canada and Global Drone and reverses on India Drone; GLO-30 is lower on India Drone, Spain, and Mozambique, by at most $0.5\,\mathrm{m}$.

4.1.4 CORS validation

Against the 4071 stations of the international GNSS CORS network, GEM-15 has the lowest DRMSE of the four models globally and on each of the six continents (Fig. 9; Table E4). Across the pooled global network, its DRMSE is $4.92\,\mathrm{m}$, 15.2 % lower than Copernicus GLO-30 ($5.80\,\mathrm{m}$) and also lower than ALOS AW3D30 and NASADEM, whereas its NMAD ($4.20\,\mathrm{m}$) is higher than that of GLO-30. By continent, the DRMSE reduction relative to GLO-30 is 16.2–23.2 % in Europe, Africa, and Oceania and 7.9–11.5 % in North America, Asia, and South America, and GEM-15 has the lowest NMAD in Europe, Oceania, and South America. ALOS AW3D30, the other optical stereo product, also has lower DRMSE than GLO-30 globally and on every continent except South America. Because CORS antennas are often mounted on pillars, masts, or building rooftops several meters above the surrounding ground (Johnston et al., 2017), a station height does not represent the mean surface of a 15 or 30 m cell, and part of each residual reflects the mount height rather than DEM error.

4.2 Digital terrain model (DTM) bare-earth evaluation

We evaluate the GEM-15 DTM against the 30 m FABDEM product (Hawker et al., 2022), which serves as our bare-earth baseline because unclassified DSMs (Copernicus GLO-30, ALOS AW3D30, and NASADEM) retain full canopy and building heights (Fig. 10; Table E2). In interpreting these results, two caveats regarding the reference data should be kept in mind. First, reference DTMs beneath dense canopies and buildings are generated by filtering out above-ground lidar returns and interpo-

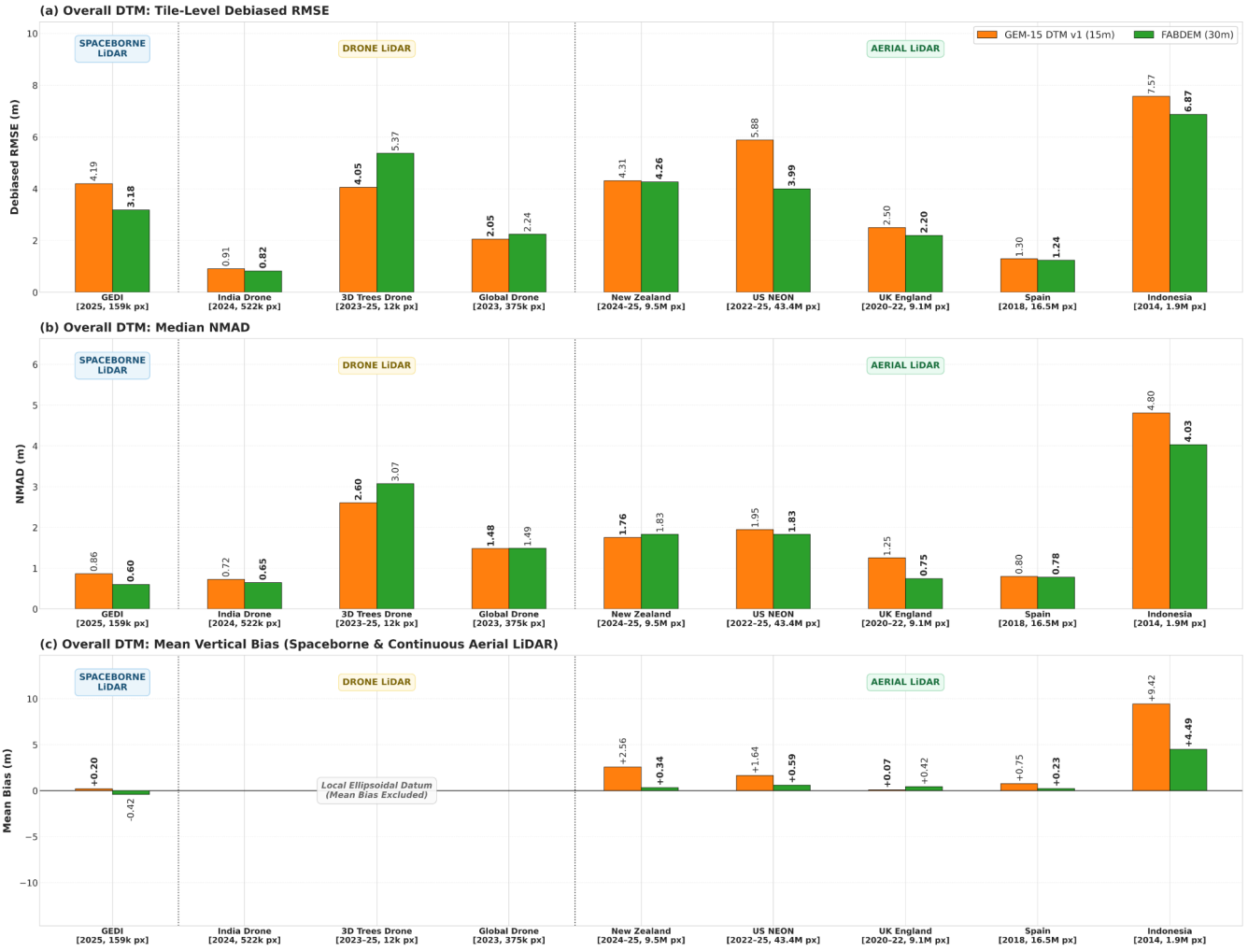


Figure 10. Overall DTM validation metrics comparing GEM-15 DTM (15 m) against FABDEM (30 m): (a) tile-level debiased root-mean-square error (DRMSE, in m), (b) normalized median absolute deviation (NMAD, in m), and (c) mean vertical bias (μ, in m).

lating across the resulting gaps rather than from direct ground measurements, introducing uncertainty. Because airborne lidar providers apply different ground-classification and interpolation algorithms, reference DTM quality varies across benchmarks; we therefore excluded the Canada, US Tropical, Brazil, and Mozambique campaigns with severe interpolation artifacts or incomplete ground returns after a visual analysis and retained the eight highest-quality airborne and drone DTM benchmarks alongside GEDI. Second, the GEDI lowest-mode ground elevation does not reliably reach the ground beneath dense canopy or buildings (Liu et al., 2021), so residual canopy remains a source of reference error in the GEDI DTM comparison even after the land-cover masking of Sect. 3.2.1. Similar to the DSM (Sect. 4.1.1), the overall GEDI DTM errors include steep footprints that published assessments typically exclude; on slopes below 5° over open ground ($\leq 5\,\mathrm{m}$ above ground), the DRMSE is $1.12\,\mathrm{m}$

for the GEM-15 DTM and $0.68\,\mathrm{m}$ for FABDEM (NMAD 0.61 vs. $0.36\,\mathrm{m}$), in line with the bare ground accuracy reported for FABDEM (Hawker et al., 2022).

On the overall DTM benchmarks (Fig. 10; Table E2), FABDEM has the lower DRMSE on most benchmarks and the GEM-15 DTM on two of the drone benchmarks (3D Trees Drone and Global Drone). The two products are within $0.1\,\mathrm{m}$ of each other on India Drone, New Zealand, and Spain, and the difference is largest where closed forest dominates: US NEON ($5.88\,\mathrm{m}$ vs. $3.99\,\mathrm{m}$), GEDI, and Indonesia. On these three benchmarks the outlier-resistant NMAD values differ by only 0.1–$0.8\,\mathrm{m}$ (FABDEM uses a GEDI-derived canopy height map as a predictor; Hawker et al. 2022), indicating that the DRMSE gap is driven mainly by tail errors in densely forested areas, where optical stereo has no direct view of the ground, rather than by the bulk of the error distribution. Overall, the GEM-15 DTM is not more accurate than FABDEM; it differs in its finer 15 m grid, more recent imagery, and exact co-registration with the GEM-15 DSM. Beneath dense canopy it also has a positive mean bias ($\mu = +9.4\,\mathrm{m}$ in Indonesia and $+1.6\,\mathrm{m}$ in US NEON; Table E2).

4.2.1 Ground vs. above-ground DTM performance ($\leq 5\,\mathrm{m}$ vs. $> 5\,\mathrm{m}$)

Stratifying the DTM evaluation by reference height above ground (bare ground and low vegetation, $\leq 5\,\mathrm{m}$, vs. sub-canopy and built structures, $> 5\,\mathrm{m}$; Table E2) shows that the GEM-15 DTM is closest to, or lower in error than, FABDEM over open ground and fragmented canopies, where the sub-meter imagery views the ground between crowns, and least accurate beneath continuous closed canopy, where it has no direct view of the ground. Over the $\leq 5\,\mathrm{m}$ stratum, the GEM-15 DTM has lower DRMSE than FABDEM on New Zealand, Global Drone, 3D Trees Drone, and Indonesia (by 8.5–17.4 %), is within $0.06\,\mathrm{m}$ of it in Spain and India Drone, and is higher in the UK, on GEDI, and in US NEON. The lower GEM-15 error on open and shrub-covered ground in Indonesia indicates that its higher overall DTM error in that survey originates mainly from the closed-canopy subset. Beneath taller canopies and buildings ($> 5\,\mathrm{m}$), GEM-15 remains lower on Global Drone and 3D Trees Drone (by 8.9–23.7 %), is within $0.25\,\mathrm{m}$ of FABDEM in the UK, India Drone, and New Zealand, and is higher in Spain, on GEDI, and in the continuous forests of US NEON ($6.68\,\mathrm{m}$ vs. $4.97\,\mathrm{m}$) and Indonesia.

4.2.2 Flat vs. steep slope DTM performance ($< 10°$ vs. $\geq 10°$)

Stratifying the DTM evaluation by terrain slope (Table E2) shows that the difference between the 15 m GEM-15 DTM and 30 m FABDEM depends on relief: on the drone and UK benchmarks the GEM-15 DTM error relative to FABDEM decreases with slope, whereas in US NEON and Indonesia and on GEDI, FABDEM remains lower on both slope classes. On flat terrain (slope $< 10°$), GEM-15 lowers DRMSE by 7.0–17.3 % on Global Drone, New Zealand, and 3D Trees Drone and performs within 0.01–$0.10\,\mathrm{m}$ in Spain and India Drone, whereas FABDEM has lower error in the UK, US NEON, Indonesia, and on GEDI. On steep slopes (slope $\geq 10°$), where 30 m cells smooth out sharp valley incisions and road cuts, GEM-15's DRMSE reductions widen to 5.8–31.8 % across the UK, India Drone, 3D Trees Drone, and Global Drone while remaining within 0.15–$0.20\,\mathrm{m}$ of FABDEM in New Zealand and Spain; FABDEM remains more accurate on steep, densely forested terrain in US NEON ($5.46\,\mathrm{m}$ vs. $8.97\,\mathrm{m}$ for GEM-15), Indonesia, and GEDI.

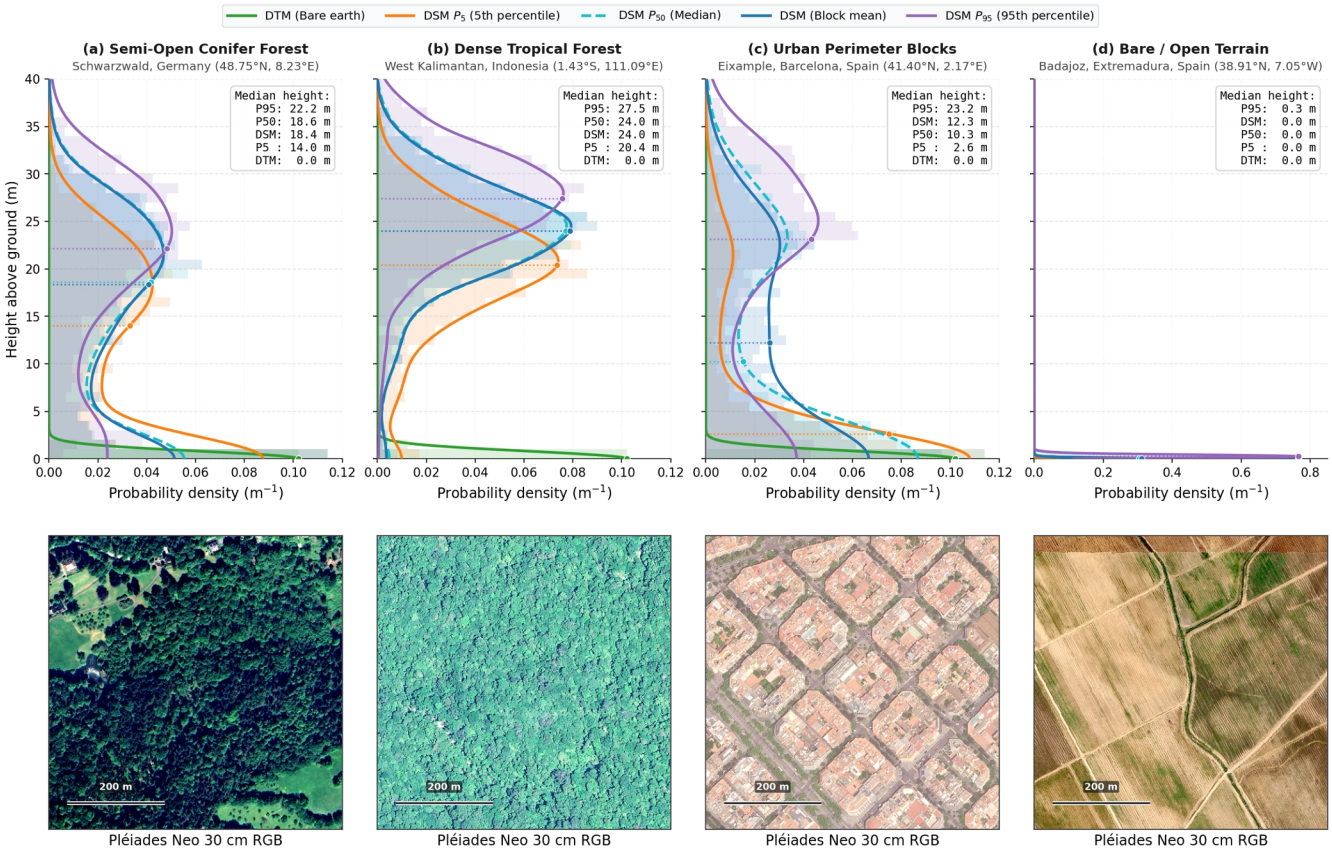


Figure 11. Height above ground distributions of the five GEM-15 elevation layers (DTM, P_5, P_{50}, DSM, and P_{95}) across four regions, with the corresponding Pléiades Neo RGB imagery shown below each plot: (a) Schwarzwald, Germany, (b) West Kalimantan, Indonesia, (c) Barcelona, Spain, and (d) Badajoz, Spain. Dotted lines and markers show the median height of each layer.

4.3 Elevation percentiles and standard deviation evaluation

To evaluate how well GEM-15 captures sub-cell vertical structure, we compare the 15 m percentile layers (P_5, P_{50}, P_{95}) and within-cell standard deviation (DSM σ_z) against the corresponding 15 m block statistics computed directly from the native 0.1–1.0 m airborne and drone lidar DSMs across all 12 benchmarks (Table E3). Because this comparison intersects only the valid-data masks of GEM-15 and the reference lidar rather than requiring valid cells across Copernicus GLO-30, ALOS AW3D30, and NASADEM simultaneously, the evaluated cell counts and DSM/DTM baseline metrics differ from the multi-model comparisons in Sects. 4.1–4.2 (most notably for US NEON, with 60.9×10^6 vs. 43.4×10^6 cells), while remaining closely aligned across the other benchmarks.

The within-cell percentiles (P_5, P_{50}, P_{95}) resolve the vertical profile of buildings and tree crowns in open and suburban terrain with errors close to those of the mean DSM, whereas under closed rainforest canopy P_5 lies well above the ground

because optical stereo has no view of it (Fig. 11; Table E3). As illustrated across four representative $600\,\mathrm{m} \times 600\,\mathrm{m}$ patches in Fig. 11, the layers separate vertically from sub-canopy gaps and street corridors (P_5) through mid-canopy and mid-block elevations (P_{50} and DSM) to upper tree crowns and rooftops (P_{95}) in semi-open forest (Fig. 11a) and urban blocks (Fig. 11c), cluster in the upper canopy above the bare-earth DTM in closed tropical forest (Fig. 11b), and collapse onto $0\,\mathrm{m}$ over bare terrain (Fig. 11d). Across the 12 benchmarks, the three percentile layers have DRMSE within $1.5\,\mathrm{m}$ of the block-mean DSM on every benchmark, spanning 1.3–$4.8\,\mathrm{m}$ (0.7–$2.8\,\mathrm{m}$ NMAD) across the temperate, semi-arid, and urban benchmarks, 4.6–$7.5\,\mathrm{m}$ in the dense tropical forests of Brazil and Indonesia, and 7.7–$8.0\,\mathrm{m}$ on the 3D Trees forest plots. In all temperate, semi-arid, and urban benchmarks except Mozambique, the NMAD is lowest for P_5 or P_{50} and highest for P_{95}, reflecting the greater fine-scale variability of emergent tree crowns and rooftop ridgelines relative to street grades and bulk canopy surfaces. Under closed canopy (Brazil and Indonesia) and in Mozambique, P_5 has the highest NMAD and DRMSE of the three percentiles, because narrow ground gaps between crowns are occluded in optical stereo views; in the UK and Spain, P_5 also has the highest DRMSE while retaining the lowest NMAD, so its error is concentrated in a tail of cells rather than in the bulk of the distribution. Across all nine airborne benchmarks, mean bias decreases monotonically from P_5 to P_{95} ($\mu(P_5) > \mu(\mathrm{DSM}) > \mu(P_{95})$ and $\mu(\sigma_z) < 0$; Table E3), because 0.5 m stereo both occludes narrow ground gaps at the base of the cell (raising P_5 relative to lidar P_5) and smooths fine-scale crown tips and rooftop peaks at the upper envelope (lowering P_{95} relative to lidar P_{95}), whereas the two effects partially cancel in the block-mean DSM and P_{50}.

Similarly, the within-cell standard deviation layer (DSM σ_z) tracks the sub-cell vertical dispersion of the native lidar DSMs (Table E3). Across the nine temperate, semi-arid, and urban benchmarks, DSM σ_z has a DRMSE of 0.66–$1.60\,\mathrm{m}$ and an NMAD of 0.32–$0.99\,\mathrm{m}$, rising in the dense, multi-layered forests of Brazil, Indonesia, and the 3D Trees plots (1.99–$3.37\,\mathrm{m}$ DRMSE; 1.64–$2.68\,\mathrm{m}$ NMAD). Together, these results indicate that the percentile and standard deviation layers capture sub-grid surface roughness and vertical stratification within each 15 m cell, with reduced fidelity beneath dense, multi-layered canopies.

5 Discussion

5.1 Resolution, temporal currency, and vertical structural distribution

Global elevation models are routinely treated as static boundary conditions (Hawker et al., 2018), even though construction, forest disturbance, and excavation continually reshape the land surface (Seto et al., 2012; Hansen et al., 2013; Maus et al., 2020). Benchmarking a modern DEM against archival airborne lidar therefore conflates sensor error with real topographic change between acquisitions. Both the multi-campaign comparison (Fig. 7) and the fixed-cohort US NEON time series (Fig. 8; Sect. 4.1.1) are consistent with this effect: the disagreement between the 2000–2015 baselines and recent lidar grows with elapsed time, whereas the GEM-15 error remains nearly constant through its 2022–2024 imagery epoch before rising between the 2023 and 2025 NEON flights. An updated elevation baseline built from 2022–2024 imagery therefore reduces, for the period it covers, the landscape change that would otherwise carry over into downstream applications.

The qualitative comparisons (Figs. 1 and 5) also illustrate that nominal grid spacing is a poor proxy for effective topographic resolution. In 30 m interferometric radar and earlier optical stereo DEMs, side-looking geometry, layover and shadow,

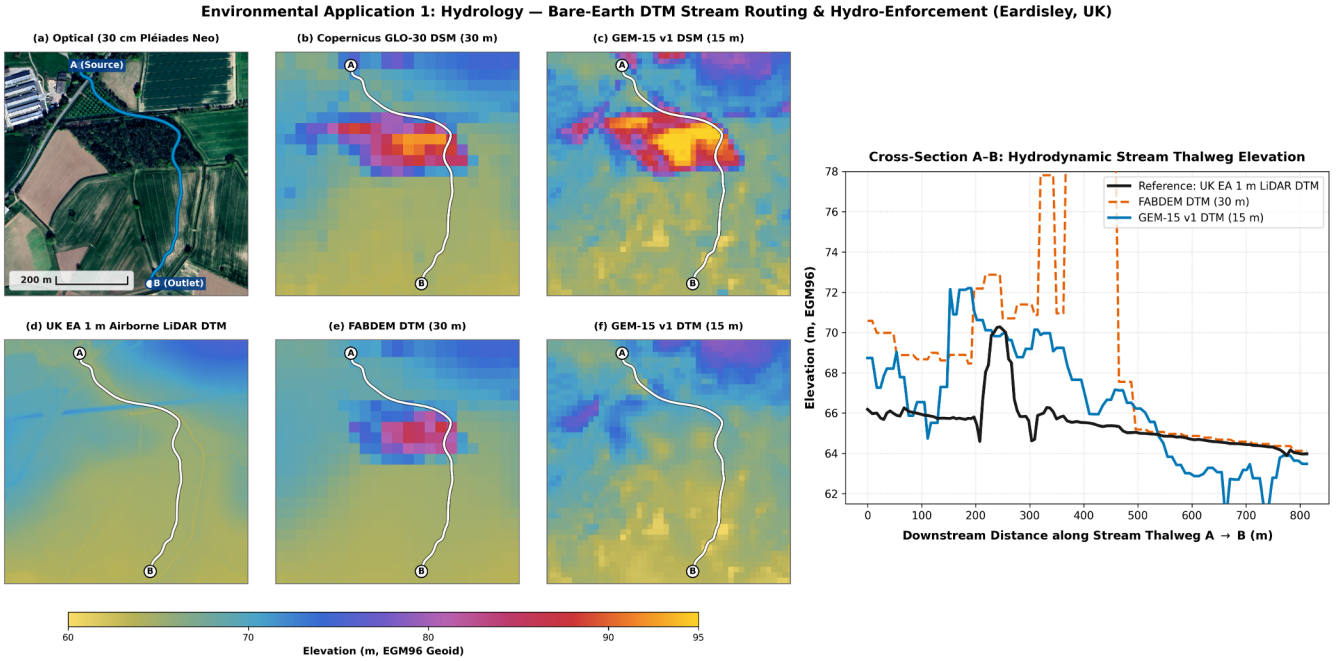


Figure 12. Stream routing comparison in Eardisley, Herefordshire, UK. Left panels (a–f) show 30 cm Pléiades Neo optical imagery with the traced stream thalweg ($A \rightarrow B$), spaceborne DSMs (Copernicus GLO-30 and GEM-15 DSM), and bare-earth DTMs (UK Environment Agency 1 m lidar reference DTM, FABDEM, and GEM-15 DTM) on a common Turbo colormap (60–95 m). The right panel shows the 1D longitudinal elevation profile along the 870 m thalweg transect $A \rightarrow B$.

and broad spatial filtering miss features well above the grid scale, often flattening urban blocks, road embankments, and incised drainage channels that were already present during acquisition. Because GEM-15 is aggregated from 0.5 m elevations reconstructed from sub-meter imagery, it preserves building edges and forest boundaries at 15 m grid spacing. The CORS comparison (Sect. 4.1.4) may reflect the same sensing difference: because many stations are mounted on rooftops and masts, a surface model that retains such elevated structures within the cell is closer to the station height, which is consistent with both optical stereo products (GEM-15 and the 30 m ALOS AW3D30) having lower DRMSE than the radar-derived GLO-30 at these stations. At the same time, a single mean height over a 225 m^2 cell averages roofs, tree crowns, and ground together. Including within-cell percentiles (P_5, P_{50}, P_{95}) and standard deviation (DSM σ_z) alongside the DTM records the height distribution inside each 15 m cell, providing globally consistent sub-grid structural statistics that have so far been available mainly from airborne lidar or, for vegetation only, from single-variable global canopy height maps (Potapov et al., 2021; Lang et al., 2023; Tolan et al., 2024).

5.2 Catchment hydrology and hydrodynamic stream routing

In catchment hydrology and 2D shallow-water flood modeling, accurate flow routing depends on preserving continuous gradients along valley floors and drainage networks (Yamazaki et al., 2019). At 30 m resolution, global elevation models frequently fail along low-order streams due to riparian canopies and channel bridging (Baugh et al., 2013; Hawker et al., 2018). Where bankside trees or hedgerows line a stream, a single 30 m pixel spans both the channel and the adjacent tree crowns. As a result, surface models record the canopy top as a ridge across the valley floor, while 30 m bare-earth models struggle to recover the bed elevation. Along the 870 m reach in Eardisley, UK (Fig. 12), a belt of riparian woodland crossing the stream produces a > 20 m artificial elevation barrier in Copernicus GLO-30. Even in FABDEM, which applies machine-learning forest removal at 30 m scale, residual vegetation artifacts of $+7.5$ m to $+12$ m remain across the thalweg ($A \rightarrow B$). Because the GEM-15 DTM is inferred at 1.0 m resolution before 15 m aggregation, it isolates the narrow stream corridor between bankside canopies, tracking the UK Environment Agency's 1 m airborne lidar DTM to within 1–$3\,\mathrm{m}$ over most of the reach (with localized residuals of $\sim$4–$6\,\mathrm{m}$ where narrow tree belts cross the channel at 150–$400\,\mathrm{m}$). In this example, the GEM-15 DTM substantially reduces the $> 20\,\mathrm{m}$ GLO-30 barrier and $+7.5$–$12\,\mathrm{m}$ FABDEM vegetation bumps along the channel; whether this holds along low-order reaches in general, and to what extent it reduces the need for stream burning or ditch carving (Lindsay, 2016), requires a systematic evaluation of hydrological conditioning that is left for future work.

5.3 Canopy edge transitions and forest structural heterogeneity

In forest ecology and terrestrial carbon accounting, coarse spatial footprints and multi-look smoothing cause 30 m elevation models to blur abrupt stand boundaries into smooth ramps, biasing biomass estimates along the forest margins where disturbance and edge mortality are concentrated (Laurance et al., 1997; Haddad et al., 2015; Brinck et al., 2017). Across a deforestation boundary in Sinop, Mato Grosso, Brazil (Fig. 13), Amazonian forest ($z \approx 380$–385 m) drops by $\sim$30 m onto cleared pasture ($z \approx 350$–355 m). Whereas Copernicus GLO-30, ALOS AW3D30, and NASADEM spread this step over a 60–100 m ramp, the GEM-15 mean DSM and P_{95} layers capture the boundary within a single 15 m pixel, while within the forest interior the auxiliary within-cell standard deviation layer (DSM σ_z; not shown) records the fine-scale structural roughness induced by selective logging and canopy gaps.

5.4 Urban morphology, building elevation, and street grades

In urban climate modeling (Stewart and Oke, 2012), wind-load engineering (Grimmond and Oke, 1999), urban canopy cover and street-level flood assessment (Schubert and Sanders, 2012), 30 m elevation rasters cannot resolve residential neighborhoods because small individual building footprints (10–15 m wide) and intervening streets fall within a single $900\,\mathrm{m}^2$ pixel. Averaging rooftops with driveways, lawns, and roads turns buildings into low mounds and fills in the streets that route surface runoff. Across the suburban residential area of Christchurch, New Zealand (Fig. 14), Copernicus GLO-30 reduces single-family dwellings and adjacent streets to a nearly uniform plane ($z \approx 6.5$–7.5 m). At 15 m grid spacing, the GEM-15 mean DSM and P_{95} resolve individual rooftops ($z \approx 10$–16 m) in close agreement with the reference LINZ 1 m airborne lidar DSM, while the

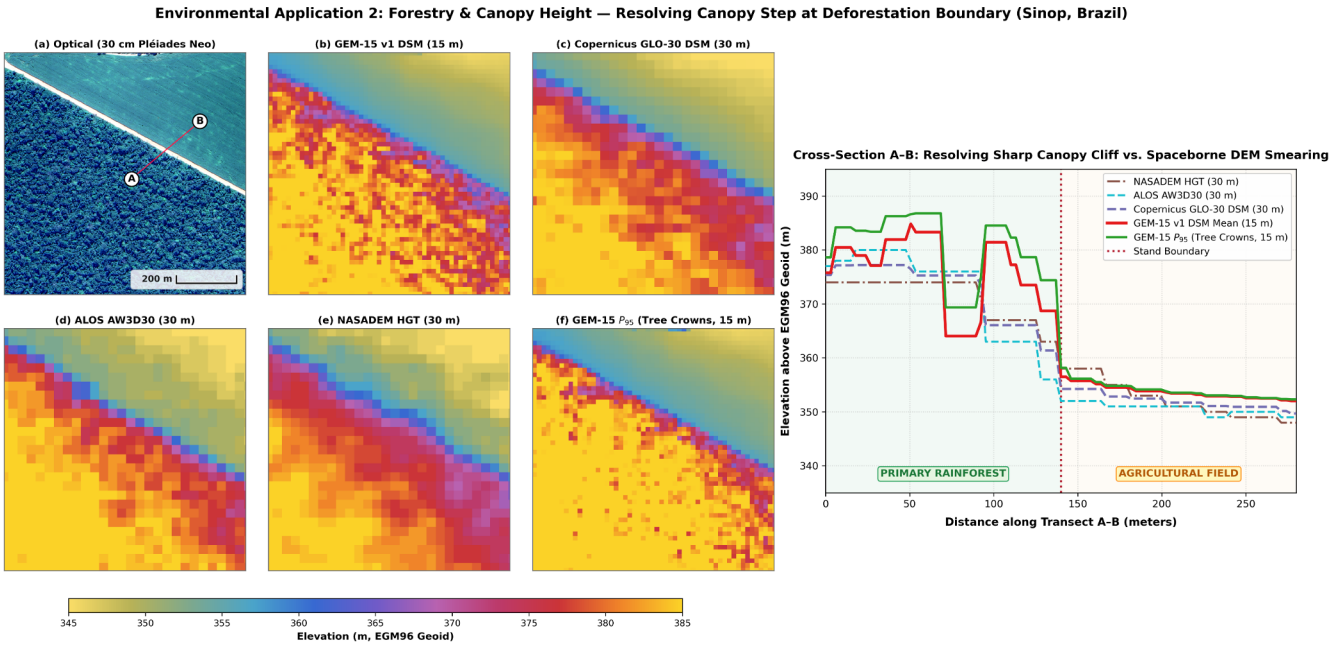


Figure 13. Deforestation boundary comparison in Sinop, Mato Grosso, Brazil. Left panels (a–f) show 30 cm Pléiades Neo optical imagery, spaceborne DSMs (GEM-15 DSM, Copernicus GLO-30, ALOS AW3D30, and NASADEM), and GEM-15 P_{95} (15 m) on a common Turbo colormap (345–385 m). The right panel shows the 1D elevation profile across the 280 m forest-to-pasture transect A–B.

5th percentile (P_5) recovers the adjacent roads ($z \approx 5.5$–6.0 m). Capturing both the roof crest (P_{95}) and street-canyon floor (P_5 and DTM) within each 15 m cell provides the vertical building geometry that may support estimates of aerodynamic roughness length for wind-load planning (Grimmond and Oke, 1999), pluvial flow corridors for urban flooding (Schubert and Sanders, 2012), and 3D building volume for urban planning (Esch et al., 2022) from a global elevation dataset.

5.5 Data limitations and future directions

GEM-15 offers finer grid spacing, more recent imagery, and sub-cell structural layers relative to the existing 30 m global DEMs, but several limitations and trade-offs should be kept in mind. GEM-15 does not cover Russia, China, Mongolia, and Greenland, where licensing restrictions on the commercial source imagery preclude production (Sect. 2.1) and the low-texture snow, ice, and desert surfaces removed by the planar-artifact filter remain voids in the product (Sect. 3.1.2). Because stereo reconstruction accuracy depends on surface texture and solar illumination, homogeneous surfaces that are not masked can still show localized surface smoothing or residual vertical error (Shean et al., 2016). Because 15 m cells differing by more than 50 m from Copernicus GLO-30 are masked (Sect. 3.1.2), surface changes (e.g., deepening open-pit mines, new high-rise buildings, or large landslides) exceeding the threshold are masked out, and the product is to that extent not independent of GLO-30. In addition, outside the 2022–2024 Pléiades Neo coverage (Sect. 2.2), cloudy equatorial and high-latitude regions

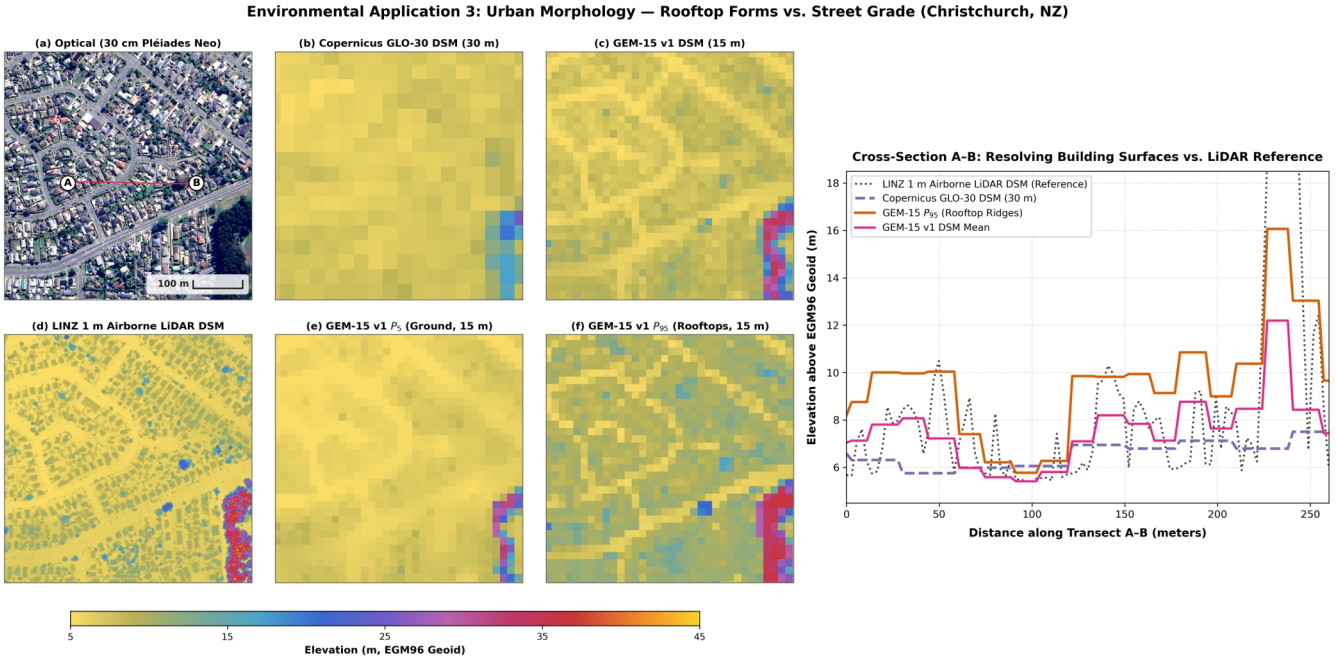


Figure 14. Suburban elevation comparison in Christchurch, New Zealand. Left panels (a–f) show 30 cm Pléiades Neo optical imagery, Copernicus GLO-30 DSM, GEM-15 DSM, LINZ 1 m airborne lidar reference DSM, and GEM-15 sub-cell percentiles (P_5 and P_{95}) on a common Turbo colormap (5–45 m). The right panel shows the 1D elevation cross-section along the 260 m residential transect A–B.

rely on older archive imagery to fill gaps. Lastly, because optical sensors do not penetrate closed forest canopies, inferring the DTM beneath dense rainforests relies on machine learning, and therefore carries greater uncertainty than products derived from active, canopy-penetrating airborne lidar. Coupling the photogrammetric elevation layers with spaceborne lidar (GEDI, Dubayah et al. 2020; ICESat-2, Markus et al. 2017; Neuenschwander and Pitts 2019) offers a direct path toward tightening sub-canopy and low-texture elevation constraints in future releases.

6 Conclusions

We have presented GEM-15, an open near-global 15 m elevation dataset reconstructed from sub-meter optical stereo satellite imagery acquired through 2024. It combines a 15 m mean DSM with within-cell percentiles (P_5, P_{50}, P_{95}), standard deviation (DSM σ_z), and a co-registered 15 m bare-earth DTM. Evaluated against GEDI spaceborne lidar, 12 airborne and drone lidar campaigns, and 4071 international GNSS CORS monuments, the GEM-15 DSM has a mean tile-debiased RMSE (DRMSE) 12.3 % lower than Copernicus GLO-30 across the lidar campaigns (3.37 m vs. 3.85 m), and lower DRMSE than ALOS AW3D30 and NASADEM on every campaign. Relative to GLO-30, GEM-15 is more accurate on most campaigns, with the largest margins over buildings and tree canopies, on steep terrain, and in recent benchmarks (up to 27 %), and less

accurate on low-relief benchmarks acquired before 2021 and over bare ground. In repeated US NEON airborne lidar acquisitions over fixed site cohorts (2016–2025), GEM-15 has the lowest DRMSE in every survey year. Although the 15 m GEM-15 DTM is not more accurate than the 30 m FABDEM globally and has positive biases beneath closed canopy, it delivers twice the resolution and is co-registered with the DSM and percentile layers. Together, these 15 m surface, percentile, and bare-earth layers provide an updated near-global elevation dataset for flood modeling, forest carbon accounting, and urban analysis, with the clearest differences from the 30 m products over built-up areas, forest edges, and recently changed landscapes.

Appendix A: Qualitative samples from lidar validation

Figures A1–A4 present representative evaluation tiles from each of the 12 UAV and airborne lidar campaigns in Table 3 (Samples A–L), comparing 30 cm Pléiades Neo optical imagery, native and 15 m block-aggregated lidar DSM and DTM ground truth (GT), the 15 m GEM-15 DSM and DTM, and the 30 m baselines on site-specific orthometric elevation scales (EGM96 geoid, in m):

- UAV lidar benchmarks (Fig. A1): In Sample A (Selangor, Malaysia), GEM-15 resolves the parallel rows of terraced housing and adjacent tree stands in the DSM while recovering the flat residential grade in the DTM. In Sample B (Karnataka, India), both the GEM-15 DSM and DTM preserve the narrow curved embankment traversing the center of the tile alongside isolated building footprints. In Sample C (Goč Forest Reserve, Serbia), the DSM captures the diagonal logging road cut through dense montane forest while the DTM reconstructs the continuous southwest-to-northeast hillside gradient.

- National airborne lidar I (Fig. A2): Sample D (Lenoir Landing, Alabama, USA) highlights dendritic drainage gullies and canopy gaps across bottomland forest. Sample E (Vancouver Crescent, Christchurch, New Zealand) shows suburban residential streets, detached single-family homes, and southeast tree stands cleanly separated between the GEM-15 DSM and DTM. Sample F (South Devon, England, UK) illustrates terraced suburban housing rows stepped along a coastal hillslope.

- National airborne lidar II (Fig. A3): Sample G (British Columbia, Canada) shows a steep montane valley wall spanning $> 150\,\mathrm{m}$ of vertical relief. Sample H (Badajoz, Spain) depicts low-relief agricultural fields bisected by a narrow north–south drainage ditch ($< 4\,\mathrm{m}$ local relief) resolved in both the GEM-15 DSM and DTM. Sample I (Manaus, Brazil) shows closed Amazonian canopy bordering a cleared northwest drainage margin, where the GEM-15 DTM removes $\sim$35–40 m of forest height to match the flat lidar plateau.

- National airborne lidar III (Fig. A4): Sample J (West Kalimantan, Indonesia) illustrates tropical forest canopy over dissected ridge-and-valley terrain. Sample K (Zambezi Delta, Mozambique) captures coastal woodland patches bordering flat deltaic marshland (where NASADEM contains unmasked voids). Sample L (Everglades National Park, Florida, USA) shows a linear east–west canal and embankment corridor cutting across low-lying subtropical mangrove forest.

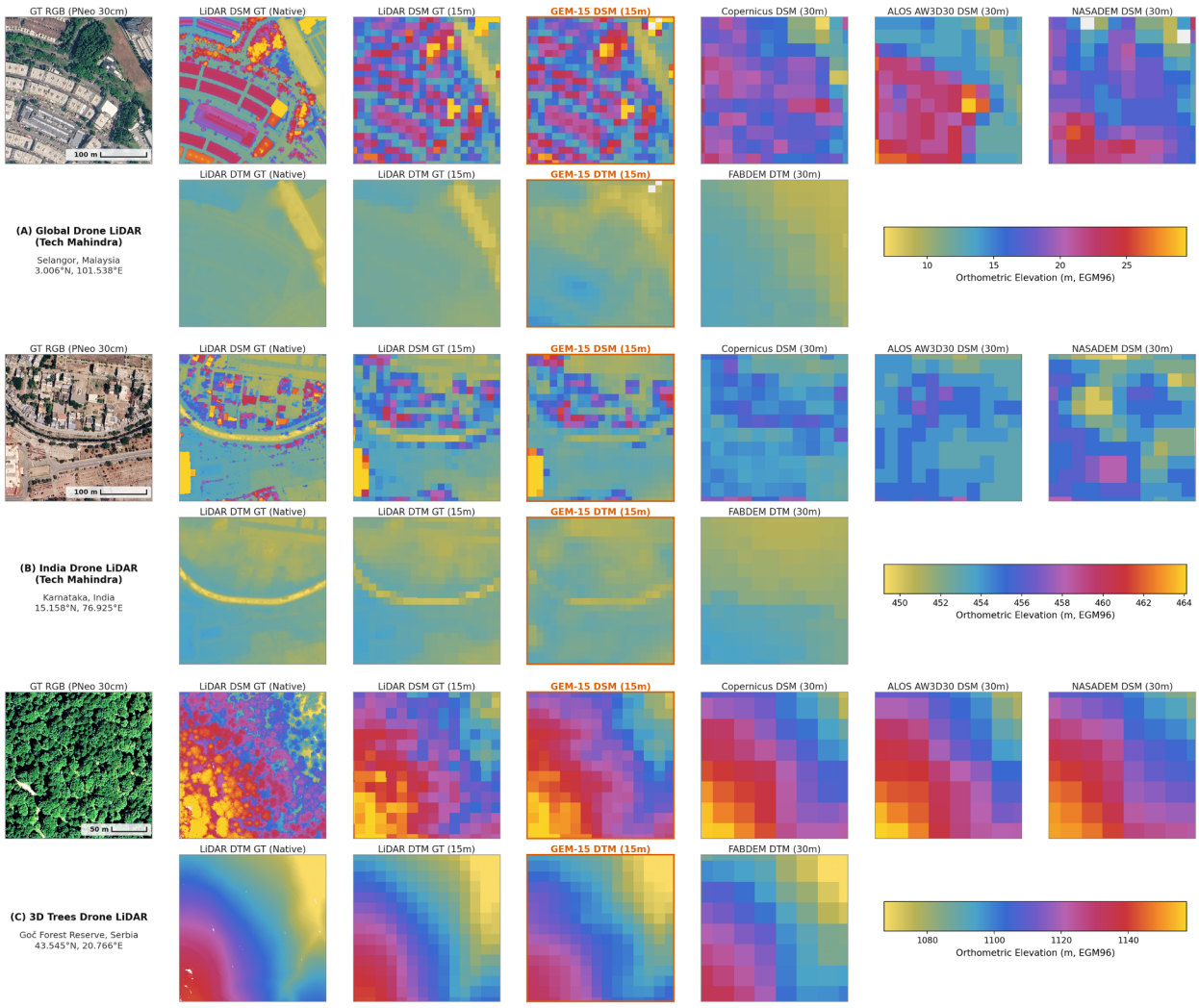


Figure A1. Qualitative benchmark comparisons across the three UAV lidar campaigns: (A) Global Drone (Selangor, Malaysia; 3.006°N, 101.538°E), (B) India Drone (Karnataka, India; 15.158°N, 76.925°E), and (C) 3D Trees Drone (Goč Forest Reserve, Serbia; 43.545°N, 20.766°E).

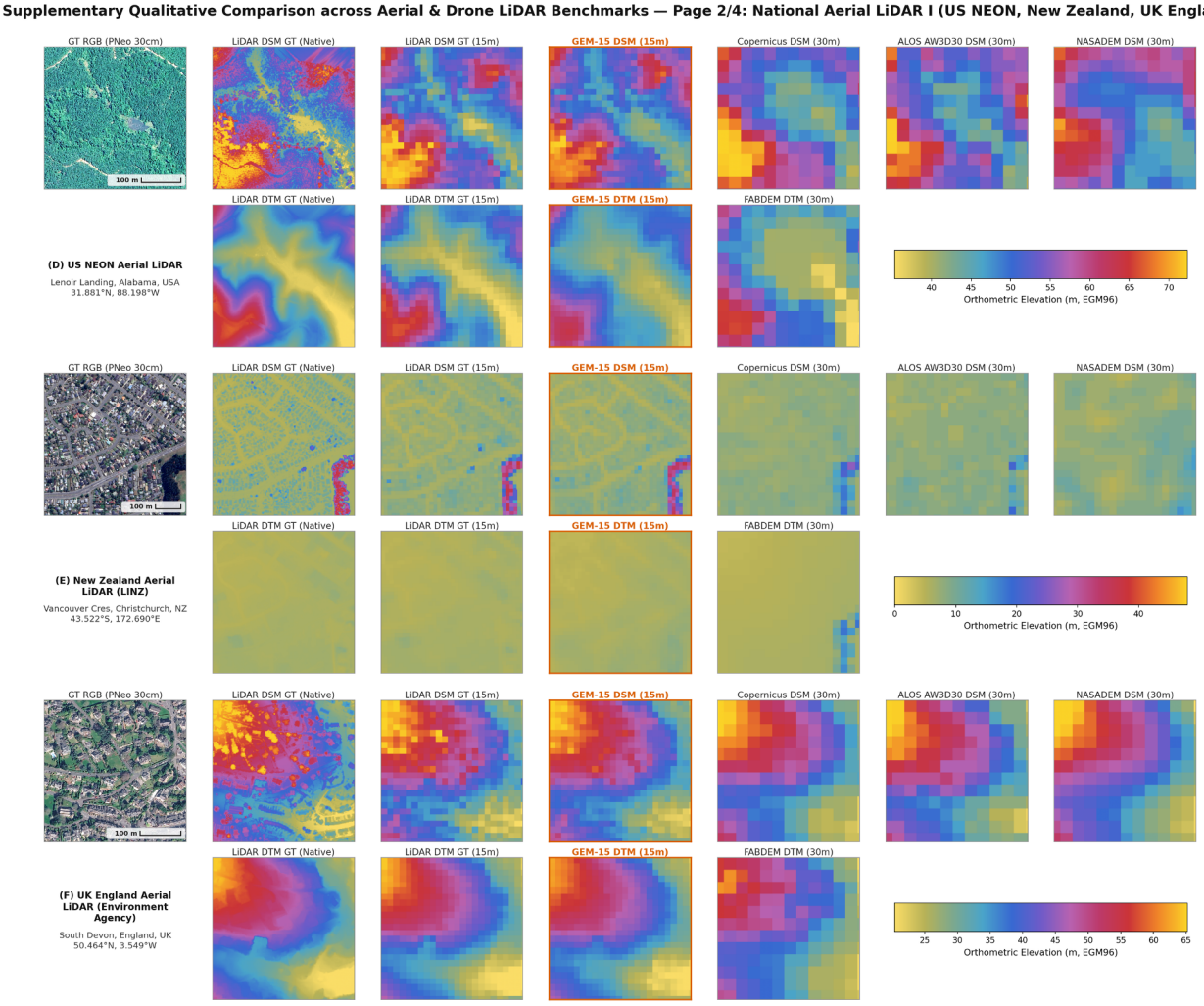


Figure A2. Qualitative benchmark comparisons across national airborne lidar campaigns (Part I): (D) US NEON (Lenoir Landing, Alabama, USA; 31.881°N, 88.198°W), (E) New Zealand LINZ (Vancouver Crescent, Christchurch, New Zealand; 43.522°S, 172.690°E), and (F) UK Environment Agency (South Devon, England, UK; 50.464°N, 3.549°W).

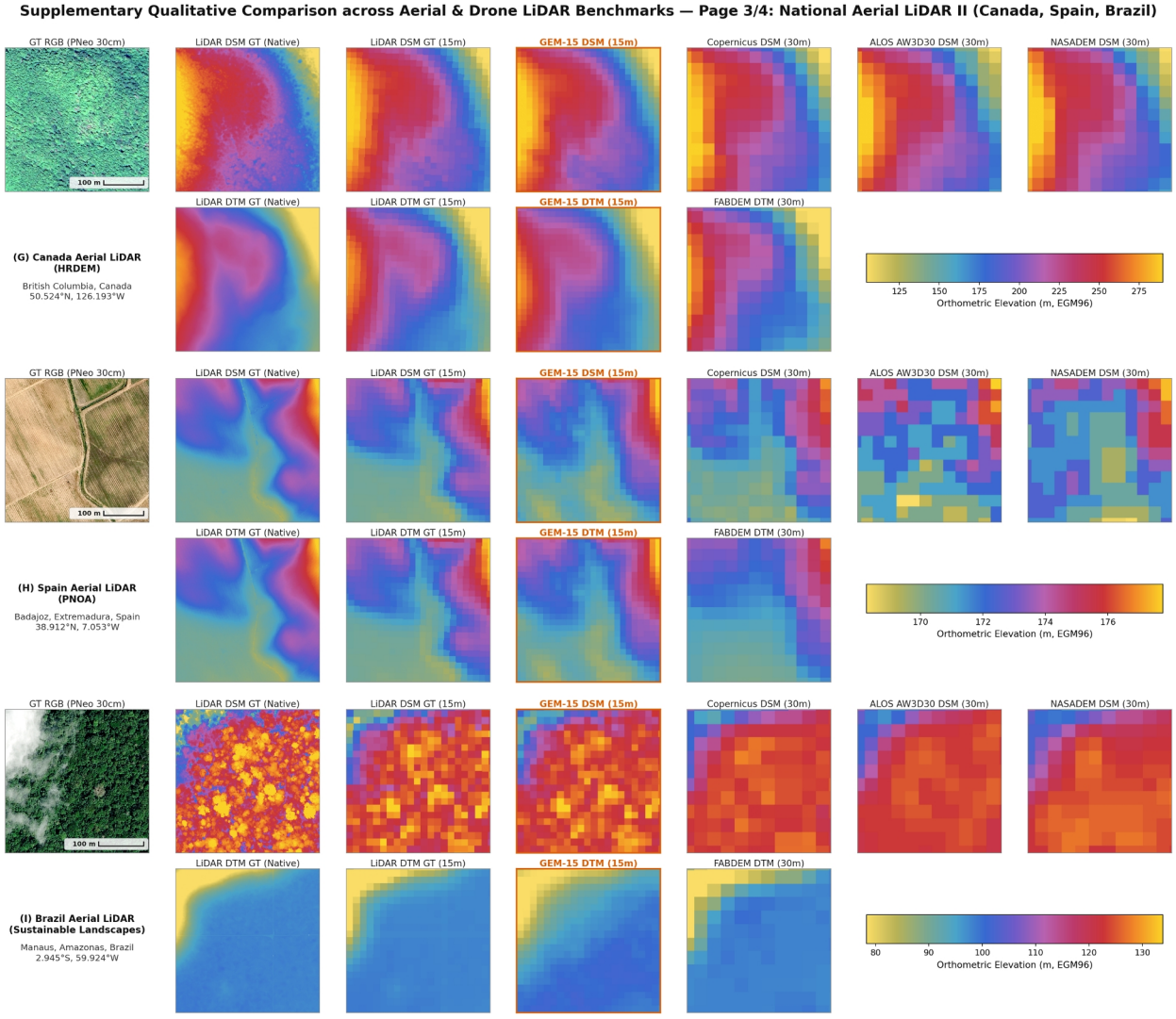


Figure A3. Qualitative benchmark comparisons across national airborne lidar campaigns (Part II): (G) Canada HRDEM (British Columbia, Canada; 50.524°N, 126.193°W), (H) Spain PNOA (Badajoz, Extremadura, Spain; 38.912°N, 7.053°W), and (I) Brazil Sustainable Landscapes (Manaus, Amazonas, Brazil; 2.945°S, 59.924°W).

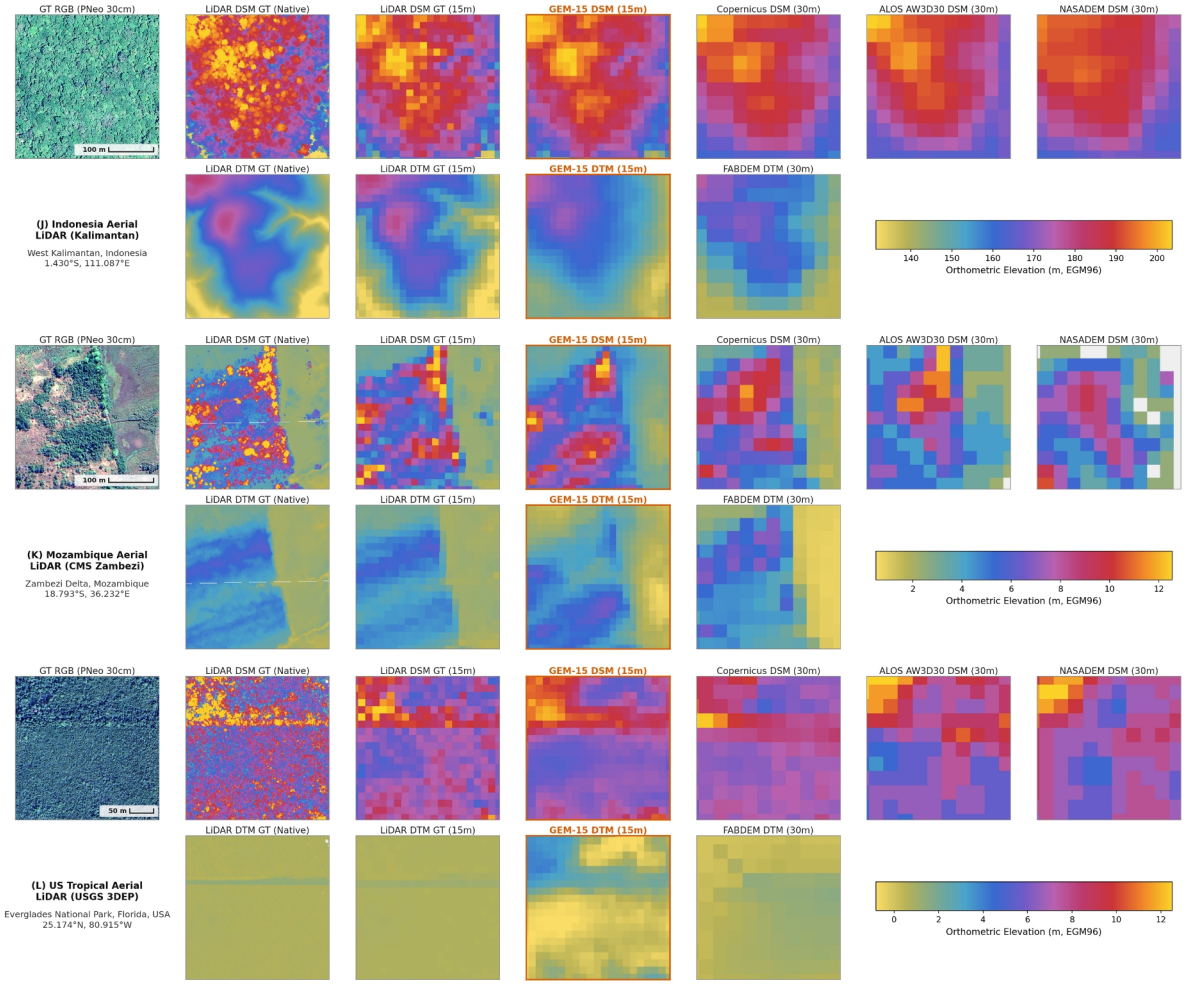


Figure A4. Qualitative benchmark comparisons across national airborne lidar campaigns (Part III): (J) Indonesia CMS Kalimantan (West Kalimantan, Indonesia; 1.430°S, 111.087°E), (K) Mozambique CMS Zambezi (Zambezi Delta, Mozambique; 18.793°S, 36.232°E), and (L) US Tropical USGS 3DEP (Everglades National Park, Florida, USA; 25.174°N, 80.915°W).

Appendix B: Two-stage hybrid spatial aggregation vs. direct sub-meter block reduction

To verify that the two-stage spatial aggregation protocol described in Sect. 3.1.2, which bilinearly resamples native $0.5\,\mathrm{m}$ reconstructions to an intermediate $2.5\,\mathrm{m}$ grid prior to $15\,\mathrm{m}$ block reduction (6×6 cells of $2.5\,\mathrm{m}$ per $15\,\mathrm{m}$ cell), does not introduce meaningful accuracy loss compared to direct $0.5\,\mathrm{m} \rightarrow 15\,\mathrm{m}$ block reduction (30×30 cells of $0.5\,\mathrm{m}$ per $15\,\mathrm{m}$ cell), we evaluated both aggregation pipelines across randomly sampled airborne and drone lidar benchmark tiles. Because the intermediate $2.5\,\mathrm{m}$ grid preserves a 36-point spatial sample within every $15\,\mathrm{m} \times 15\,\mathrm{m}$ cell, the resulting $15\,\mathrm{m}$ DSM, DTM, percentiles (P_5, P_{50}, P_{95}), and standard deviation (DSM σ_z) achieve nearly identical lidar validation accuracy to direct $0.5\,\mathrm{m}$ block reduction, within $0.02\,\mathrm{m}$ DRMSE across all six bands and within $0.01\,\mathrm{m}$ NMAD for the DSM and DTM ($0.04\,\mathrm{m}$ NMAD for the percentiles and $0.13\,\mathrm{m}$ for DSM σ_z), while reducing global memory and compute overhead by more than an order of magnitude.

Appendix C: Native high-resolution samples of GEM-15 DSMs and DTMs

Figure C1 shows examples of the native sub-meter GEM-15 DSM and DTM reconstructions (Sect. 3.1.1) alongside 1 m lidar ground truth and the final 15 m aggregated layers across three residential and urban sites. At native resolution, the 0.5 m DSM resolves detached houses and garden trees in Christchurch (Fig. C1A), multi-story courtyard buildings in Shah Alam (Fig. C1B), and tightly spaced townhome rows and warehouses in Nonthaburi (Fig. C1C), closely matching the 1 m lidar DSMs. Estimating bare-earth elevation at 1.0 m before downsampling removes these buildings and tree crowns to recover the underlying ground slope and street corridors, while the sub-cell height distribution of the native DSM is retained at 15 m through the percentile (P_5, P_{50}, P_{95}) and standard deviation (DSM σ_z) layers.

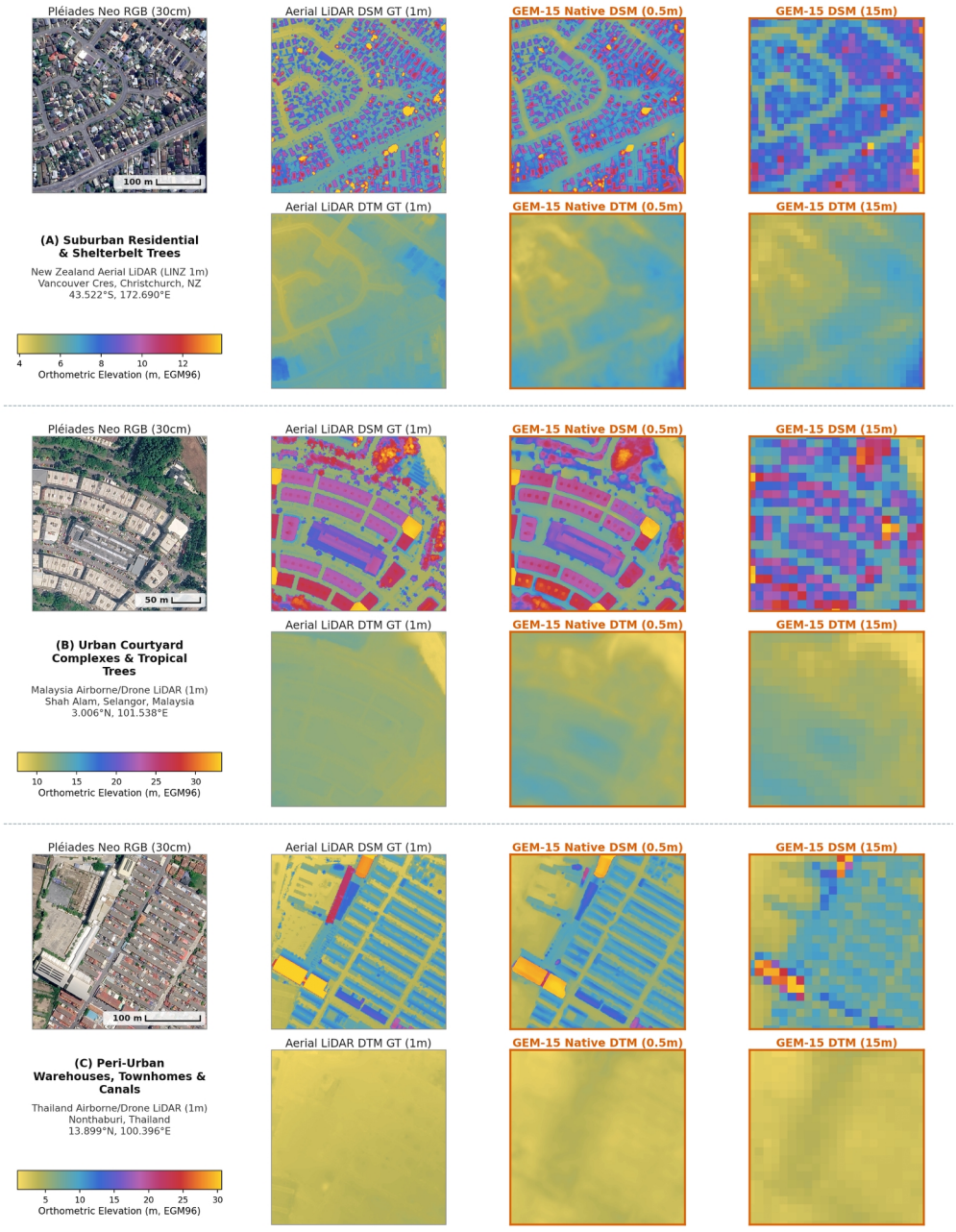


Figure C1. Comparison of intermediate native-resolution GEM-15 reconstructions against 1 m lidar ground truth (GT) and aggregated 15 m GEM-15 layers across three locations. Top row per site (left to right): Pléiades Neo 30 cm RGB, 1 m lidar DSM GT, native GEM-15 DSM (0.5 m), and GEM-15 DSM (15 m); bottom row: elevation colorbar (m, EGM96), 1 m lidar DTM GT, native GEM-15 DTM, and GEM-15 DTM (15 m).

Appendix D: Commissioned Tech Mahindra UAV validation datasets

To evaluate GEM-15 across dense urban, peri-urban, and agricultural landscapes in regions where open national airborne lidar is unavailable, we incorporate two proprietary UAV reference datasets commissioned by Google Research and collected by Tech Mahindra Limited: Tech Mahindra India Drone-lidar (August–October 2024) and Tech Mahindra Global Drone-lidar (June 2023).

D1 Geographic coverage and site selection

- Tech Mahindra India Drone-lidar (August–October 2024): Covers 522×10^3 valid $15\,\mathrm{m} \times 15\,\mathrm{m}$ evaluation cells ($\approx 117.4\,\mathrm{km}^2$ within $\approx 120\,\mathrm{km}^2$ of commissioned $1\,\mathrm{km} \times 1\,\mathrm{km}$ tiles) distributed across 15 tier-1 and tier-2 cities spanning five Indian states: Hyderabad, Warangal, Hanamkonda, and Suryapet (Telangana); Ballari, Tumakuru, and Mandya (Karnataka); Chennai (Tamil Nadu); Anantapur, Guntur, Kurnool, and Vizianagaram (Andhra Pradesh); and Brahmapur, Baripada, and Puri (Odisha). Survey blocks were selected to sample representative 1- to 5-story residential and commercial building morphology alongside peri-urban and agricultural fringes.

- Tech Mahindra Global Drone-lidar (June 2023): Covers 375×10^3 valid $15\,\mathrm{m} \times 15\,\mathrm{m}$ evaluation cells ($\approx 84.4\,\mathrm{km}^2$) across 64 urban and peri-urban survey areas distributed across 10 countries spanning Latin America, Africa, the Middle East, and Asia: Chile (6 areas), Peru (6 areas), Nigeria (7 areas), Morocco (6 areas), Turkey (6 areas), Malaysia (6 areas), Thailand (7 areas), the Philippines (7 areas), Taiwan (7 areas), and South Korea (6 areas).

D2 Acquisition protocol, processing, and licensing

Both collections were acquired under clear-sky conditions (no clouds or haze, and solar elevation $> 30°$, or $> 40°$ in dense urban centers) using low-altitude UAVs flown in a high-overlap cross-grid pattern ($\sim$ 180–200 captures per km^2 with perimeter buffers to prevent edge stitching artifacts). Trajectories were georeferenced against local Differential GPS (DGPS) base stations to generate co-registered $7.5\,\mathrm{cm}$ true-orthorectified RGB imagery (8-bit GeoTIFF) and 0.25–$0.30\,\mathrm{m}$ DSM and bare-earth DTM rasters (32-bit `Float32` GeoTIFF). For the India survey, in accordance with the Government of India's National Geospatial Policy, absolute coordinates incorporate a regulatory offset (1–$3\,\mathrm{m}$ horizontal, 3–$5\,\mathrm{m}$ vertical) while preserving local relative surface and terrain geometry; this block-level vertical offset is removed by the tile-level debiasing (Bias_k, Eq. 1) prior to computing DRMSE and NMAD.

Both datasets were acquired under commercial third-party licensing agreements that restrict sharing of raw and aggregated reference rasters beyond internal validation and prohibit public redistribution.

Appendix E: Detailed quantitative benchmark tables

Tables E1–E4 report the complete numerical validation results summarized in Sect. 4. All metrics are given in meters and follow the definitions in Sect. 3.2: the tile-debiased RMSE (DRMSE) and NMAD remove the local mean or median offset within each $1.5\,\mathrm{km} \times 1.5\,\mathrm{km}$ evaluation tile, whereas the bias is the pooled mean of DEM − reference across all valid cells. The "Cells" column lists the number of valid $15\,\mathrm{m}$ cells ($25\,\mathrm{m}$ cells for GEDI) shared across the compared products, and the best model for each metric and stratum is shown in bold. In Tables E1–E3, bias is omitted for the three drone campaigns georeferenced to local survey datums (Sect. 3.2.2), and the summary row at the bottom gives the unweighted mean across the airborne campaigns.

Table E1 compares the GEM-15 DSM against Copernicus GLO-30, ALOS AW3D30, and NASADEM across spaceborne GEDI and all 12 aerial lidar benchmarks (overall values in Fig. 6), both overall and stratified by reference height above ground ($> 5\,\mathrm{m}$ vs. $\leq 5\,\mathrm{m}$) and terrain slope ($< 10^\circ$ vs. $\geq 10^\circ$; the steep stratum is empty in the low-relief US Tropical survey). Because each stratum is debiased independently within every tile, the overall DRMSE retains vertical offsets between strata and can exceed that of both constituent strata. Table E2 reports the same breakdown for the GEM-15 DTM and FABDEM across GEDI and the eight lidar campaigns with reliable bare-earth reference DTMs (Fig. 10); for GEDI, the footprint count is smaller than in Table E1 (101×10^3 vs. 159×10^3) because tree-covered, built-up, and water classes are masked out (Sect. 3.2.1). Table E3 evaluates all six GEM-15 layers against the corresponding $15\,\mathrm{m}$ block statistics of the native lidar rasters (Sect. 4.3), with DTM entries omitted for the four campaigns excluded from Table E2 (Sect. 4.2). Because this comparison intersects only the valid masks of GEM-15 and the reference lidar, the cell counts are slightly different than in Table E1; in addition, part of the systematic bias across P_5, P_{95}, and DSM σ_z reflects the coarser $2.5\,\mathrm{m}$ sub-cell support of the GEM-15 statistics relative to the native 0.1–$1.0\,\mathrm{m}$ lidar. Finally, Table E4 lists the GNSS CORS comparisons globally and by continent (Fig. 9), where station residuals are debiased by the global mean offset for the global row and by each continent's mean offset for the continental rows (Sect. 3.2.3).

Table E1. DSM validation summary across spaceborne GEDI and 12 airborne and drone lidar benchmarks. All metrics are in m, with the best model per metric in each stratum shown in bold. Dashes (—) indicate strata with no cells (steep terrain in US Tropical) or omitted local-datum drone biases. The "Mean (Airborne + Drone)" row is the unweighted mean over the lidar campaigns with an entry in each column (GEDI excluded), and its cell count is the total number of evaluated cells.

Benchmark	Cells	Metric	Overall				Above-ground (> 5 m)				Ground (≤ 5 m)				Flat (< 10°)				Steep (≥ 10°)			
			GEM-15	GLO-30	ALOS	NASADEM	GEM-15	GLO-30	ALOS	NASADEM	GEM-15	GLO-30	ALOS	NASADEM	GEM-15	GLO-30	ALOS	NASADEM	GEM-15	GLO-30	ALOS	NASADEM
GEDI (Spaceborne)	159k	DRMSE	**5.05**	5.10	5.35	5.86	**6.32**	6.35	6.62	7.18	1.61	**1.34**	1.62	2.25	3.71	**3.68**	3.92	4.25	**7.86**	8.03	8.33	9.18
		NMAD	1.78	**1.60**	2.10	2.82	3.54	**3.43**	3.73	4.28	0.69	**0.46**	0.91	1.49	1.26	**1.00**	1.53	2.19	**5.51**	5.54	5.79	6.63
		Bias	**-6.89**	-7.67	-6.90	-8.43	-9.86	-10.43	**-9.85**	-11.82	**-3.49**	-4.51	-3.53	-4.55	**-5.75**	-6.77	-5.96	-7.28	-10.86	-10.85	**-10.21**	-12.47
India Drone	522k	DRMSE	**2.23**	2.79	2.91	3.35	**2.70**	2.81	3.06	3.13	1.76	**1.16**	1.35	1.81	**2.21**	2.77	2.89	3.33	5.53	**5.04**	5.19	5.49
		NMAD	**1.53**	2.12	2.18	2.88	**1.95**	1.98	2.26	2.46	1.59	**0.94**	1.19	1.62	**1.53**	2.12	2.18	2.87	2.23	**2.17**	2.51	2.85
		Bias	—	—	—	—	—	—	—	—	—	—	—	—	—	—	—	—	—	—	—	—
3D Trees Drone	12k	DRMSE	**6.66**	6.88	7.93	7.91	**5.85**	6.25	6.99	7.30	5.02	**4.27**	5.50	4.88	5.32	**5.28**	6.33	5.81	**6.31**	6.84	7.94	7.99
		NMAD	**4.62**	5.64	6.55	7.18	**5.62**	5.93	6.26	7.92	1.58	**1.40**	2.55	3.13	**2.64**	2.70	3.37	4.11	**5.27**	6.52	6.75	8.44
		Bias	—	—	—	—	—	—	—	—	—	—	—	—	—	—	—	—	—	—	—	—
Global Drone	375k	DRMSE	**3.05**	3.89	4.09	4.45	**3.68**	4.32	4.60	4.63	2.65	**2.32**	2.68	2.77	**3.00**	3.84	4.04	4.40	**3.27**	4.12	4.54	4.88
		NMAD	**2.16**	2.88	2.98	3.56	**2.61**	3.04	3.40	3.58	2.12	**1.68**	2.01	2.25	**2.13**	2.84	2.94	3.52	**2.46**	3.32	3.60	4.22
		Bias	—	—	—	—	—	—	—	—	—	—	—	—	—	—	—	—	—	—	—	—
New Zealand	9.5M	DRMSE	**3.92**	5.37	5.70	6.82	**4.51**	6.38	6.95	8.60	**2.87**	3.26	3.46	4.54	**2.64**	3.57	3.97	4.44	**4.62**	6.32	6.64	8.10
		NMAD	**1.50**	2.03	3.04	4.07	**3.03**	4.40	5.00	7.05	1.07	**0.97**	2.04	2.72	0.90	**0.80**	1.91	2.26	**2.15**	3.36	4.27	6.29
		Bias	0.55	-1.87	**0.08**	-1.80	**-1.39**	-5.45	-3.59	-5.22	2.32	0.78	2.78	**0.75**	1.01	-1.03	1.13	**-0.30**	**0.20**	-2.52	-0.73	-2.96
US NEON	43.4M	DRMSE	**4.00**	4.66	5.27	5.84	**4.99**	5.39	5.97	6.37	**2.44**	2.88	2.89	3.52	**3.51**	4.02	4.54	4.99	**4.77**	5.69	6.44	7.19
		NMAD	**1.78**	1.95	2.59	3.80	**3.63**	3.74	4.52	5.18	0.98	**0.72**	1.27	2.35	1.40	**1.30**	2.00	3.15	**2.74**	3.14	3.88	5.33
		Bias	-1.23	-1.25	**-0.83**	-3.26	-4.66	**-3.28**	-4.46	-7.52	1.59	0.49	2.14	**0.19**	-1.10	-1.58	**-1.03**	-3.40	-1.52	-0.59	**-0.42**	-3.00
Canada	4.8M	DRMSE	**3.61**	3.95	4.36	5.08	4.48	**4.36**	4.71	5.28	1.83	**1.79**	2.33	2.35	**3.23**	3.66	3.97	4.62	**4.79**	4.89	5.59	6.54
		NMAD	1.71	**1.62**	2.41	3.00	3.54	**3.50**	3.94	4.55	0.90	**0.40**	1.27	1.48	1.42	**1.12**	2.00	2.53	**3.42**	3.58	4.43	5.29
		Bias	-4.80	**-2.34**	-3.06	-4.37	-7.77	**-5.00**	-7.02	-8.79	-1.58	0.63	0.95	**0.02**	-3.99	**-2.10**	-2.23	-3.69	-8.22	**-3.35**	-6.56	-7.20
UK England	9.0M	DRMSE	**2.33**	2.36	3.04	3.03	**4.07**	4.25	4.57	4.12	2.16	**1.72**	2.48	2.12	2.20	**2.17**	2.88	2.78	**3.06**	3.52	4.10	4.49
		NMAD	1.18	**0.61**	1.76	1.62	**3.42**	3.45	3.85	3.56	1.11	**0.53**	1.48	1.35	1.12	**0.54**	1.67	1.50	**1.69**	1.72	2.66	3.27
		Bias	0.21	**-0.18**	0.32	-0.30	**0.06**	-2.54	-2.84	-5.07	0.67	**0.56**	1.16	0.74	**0.16**	-0.18	0.33	-0.26	0.62	**-0.19**	0.19	-0.66
US Tropical	1.4M	DRMSE	1.33	**1.19**	1.85	1.85	1.96	**1.77**	2.50	2.28	0.93	**0.75**	1.20	1.37	1.14	**0.98**	1.71	1.72	—	—	—	—
		NMAD	0.78	**0.70**	1.18	1.56	1.15	**0.95**	1.92	1.72	0.58	**0.43**	0.99	1.42	0.76	**0.69**	1.16	1.55	—	—	—	—
		Bias	1.86	-1.57	**0.08**	-1.68	**0.78**	-2.59	-1.74	-2.66	3.62	0.17	1.96	**0.05**	1.80	-1.63	**0.03**	-1.75	—	—	—	—
Spain	16.5M	DRMSE	1.39	**1.34**	1.68	2.30	3.06	**2.35**	2.63	3.02	1.23	**1.09**	1.21	2.06	1.22	**1.19**	1.47	2.04	1.88	**1.75**	2.30	3.12
		NMAD	0.85	**0.66**	1.16	1.83	2.22	**1.69**	1.87	2.54	0.78	**0.60**	0.87	1.67	0.79	**0.55**	1.04	1.69	**1.14**	1.26	1.86	2.64
		Bias	0.66	**-0.22**	0.82	-1.10	**-1.53**	-3.20	-3.90	-5.53	1.47	0.61	1.70	**-0.23**	0.71	**-0.16**	0.93	-0.98	0.42	-0.48	**0.32**	-1.65
Brazil	1.1M	DRMSE	**4.20**	4.68	4.89	5.46	**4.18**	4.64	4.85	5.41	2.18	**2.18**	2.82	4.27	**4.35**	4.79	4.98	5.51	**3.10**	4.07	4.40	5.33
		NMAD	**2.85**	3.62	3.96	4.69	**2.86**	3.60	3.95	4.66	**1.26**	1.76	2.44	3.20	**2.96**	3.70	4.01	4.70	**2.32**	3.38	3.90	4.87
		Bias	-2.25	-1.25	**-0.32**	-1.97	-2.29	-1.32	**-0.42**	-2.10	**3.01**	8.07	12.04	14.06	-2.20	-1.22	**-0.29**	-1.79	-2.84	-1.31	**-0.34**	-2.80
Indonesia	1.9M	DRMSE	**6.06**	7.52	8.04	9.20	**6.22**	7.65	8.11	9.20	**4.38**	5.12	5.81	5.52	**4.74**	5.17	5.74	6.74	**7.06**	9.24	9.76	11.06
		NMAD	**3.48**	4.13	5.14	6.53	**3.75**	4.59	5.34	6.66	1.40	**0.56**	1.85	2.58	2.35	**2.06**	3.06	3.91	**4.95**	7.57	8.39	10.48
		Bias	**0.45**	-2.42	-2.22	-4.25	**-0.06**	-2.89	-2.87	-5.27	6.25	**2.98**	4.67	5.64	**0.90**	-1.90	-1.84	-3.70	**-0.11**	-3.04	-2.70	-4.92
Mozambique	8.8M	DRMSE	1.69	**1.53**	2.43	2.53	1.68	**1.56**	2.67	2.37	2.09	**1.39**	1.96	1.87	1.69	**1.53**	2.43	2.53	1.65	**1.56**	1.74	2.49
		NMAD	1.28	**1.18**	1.92	2.19	1.38	**1.29**	2.26	2.12	1.62	**1.04**	1.36	1.63	1.28	**1.18**	1.92	2.19	1.65	1.67	**1.56**	3.00
		Bias	1.23	-1.17	**-0.33**	-2.72	1.44	-1.73	**-0.39**	-3.97	2.65	1.19	1.40	**0.46**	1.23	-1.16	**-0.33**	-2.73	**-1.32**	-1.61	-1.64	-3.32
Mean (Airborne)	97.4M	DRMSE	**3.37**	3.85	4.35	4.82	**3.95**	4.31	4.80	5.14	2.46	**2.33**	2.81	3.09	**2.94**	3.25	3.75	4.08	**4.19**	4.82	5.33	6.06
		NMAD	**1.98**	2.26	2.90	3.58	**2.93**	3.18	3.71	4.33	1.25	**0.92**	1.61	2.12	**1.61**	1.63	2.27	2.83	**2.73**	3.43	3.98	5.15
		Bias	**-0.37**	-1.36	-0.61	-2.38	**-1.71**	-3.11	-3.03	-5.12	2.22	**1.72**	3.20	2.41	**-0.16**	-1.22	-0.37	-2.07	-1.60	-1.64	**-1.49**	-3.31

Table E2. Bare-earth DTM validation summary comparing GEM-15 DTM (15 m) and FABDEM (30 m) across spaceborne GEDI (2025), three UAV lidar benchmarks, and five national airborne lidar campaigns (Canada, US Tropical, Brazil, and Mozambique are excluded because of reference DTM quality; Sect. 4.2). All metrics are in m, with the best model per metric in each stratum shown in bold. The "Mean (Airborne + Drone)" row is the unweighted mean over the lidar campaigns with an entry in each column (GEDI excluded), and its cell count is the total number of evaluated cells.

Benchmark	Cells	Metric	Overall		Above-ground (> 5 m)		Ground (≤ 5 m)		Flat ($< 10°$)		Steep ($\geq 10°$)	
			GEM-15 DTM	FABDEM	GEM-15 DTM	FABDEM	GEM-15 DTM	FABDEM	GEM-15 DTM	FABDEM	GEM-15 DTM	FABDEM
GEDI (Spaceborne)	101k	DRMSE	4.19	**3.18**	7.10	**5.35**	1.42	**1.05**	1.67	**1.45**	9.75	**7.35**
		NMAD	0.86	**0.60**	1.79	**1.76**	0.66	**0.41**	0.71	**0.47**	**4.51**	4.66
		Bias	**0.20**	-0.42	0.65	**0.19**	**0.00**	-0.70	**0.27**	-0.51	-0.20	**0.11**
India Drone	522k	DRMSE	0.91	**0.82**	0.91	**0.80**	0.88	**0.82**	0.89	**0.79**	**2.57**	2.90
		NMAD	0.72	**0.65**	0.77	**0.64**	0.69	**0.64**	0.72	**0.64**	**1.85**	2.06
		Bias	—	—	—	—	—	—	—	—	—	—
3D Trees Drone	12k	DRMSE	**4.05**	5.37	**4.03**	5.28	**3.02**	3.49	**2.83**	3.42	**4.41**	5.96
		NMAD	**2.60**	3.07	**3.64**	4.31	**1.20**	1.55	**1.50**	1.69	**3.35**	4.49
		Bias	—	—	—	—	—	—	—	—	—	—
Global Drone	375k	DRMSE	**2.05**	2.24	**2.04**	2.24	**2.01**	2.21	**1.99**	2.14	**2.32**	3.40
		NMAD	**1.48**	1.49	1.47	**1.46**	**1.43**	1.47	1.44	**1.44**	**1.91**	2.99
		Bias	—	—	—	—	—	—	—	—	—	—
New Zealand	9.5M	DRMSE	4.31	**4.26**	5.73	**5.48**	**2.80**	3.06	**2.39**	2.61	5.28	**5.13**
		NMAD	**1.76**	1.83	4.50	**4.37**	1.06	**1.04**	0.90	**0.73**	**3.04**	3.42
		Bias	2.56	**0.34**	4.78	**1.00**	1.37	**-0.02**	1.78	**0.21**	3.16	**0.43**
US NEON	43.4M	DRMSE	5.88	**3.99**	6.68	**4.97**	4.73	**2.67**	3.46	**3.00**	8.97	**5.46**
		NMAD	1.95	**1.83**	4.43	**3.68**	0.99	**0.90**	1.39	**1.22**	3.91	**3.76**
		Bias	1.64	**0.59**	2.42	**1.64**	1.05	**-0.21**	1.51	**0.43**	1.93	**0.92**
UK England	9.0M	DRMSE	2.50	**2.20**	3.66	**3.62**	1.88	**1.54**	2.26	**1.82**	**3.59**	3.81
		NMAD	1.25	**0.75**	**2.57**	2.73	1.11	**0.62**	1.18	**0.67**	**1.98**	1.99
		Bias	**0.07**	0.42	**2.95**	3.38	-0.29	**0.04**	**0.00**	0.31	**0.72**	1.40
Spain	16.5M	DRMSE	1.30	**1.24**	2.74	**2.04**	1.21	**1.19**	**1.06**	1.07	1.94	**1.74**
		NMAD	0.80	**0.78**	1.79	**1.59**	0.78	**0.76**	0.73	**0.70**	**1.18**	1.25
		Bias	0.75	**0.23**	1.36	**1.24**	0.74	**0.20**	0.79	**0.24**	0.59	**0.20**
Indonesia	1.9M	DRMSE	7.57	**6.87**	7.81	**6.99**	**3.95**	4.78	4.69	**4.29**	9.62	**8.68**
		NMAD	4.80	**4.03**	5.51	**4.57**	1.05	**0.46**	2.16	**1.32**	9.03	**8.21**
		Bias	9.42	**4.49**	10.09	**4.89**	4.09	**1.32**	10.38	**5.34**	8.40	**3.62**
Mean (Airborne)	81.4M	DRMSE	3.57	**3.37**	4.20	**3.93**	2.56	**2.47**	2.45	**2.39**	4.84	**4.63**
		NMAD	1.92	**1.80**	3.09	**2.92**	1.04	**0.93**	1.25	**1.05**	**3.28**	3.52
		Bias	2.89	**1.21**	4.32	**2.43**	1.39	**0.27**	2.89	**1.30**	2.96	**1.31**

Table E3. Sub-cell vertical profile validation of the six GEM-15 layers across the 12 UAV and airborne lidar benchmarks (Sect. 4.3). Each GEM-15 layer is evaluated against the corresponding $15\,\mathrm{m}$ reference lidar block statistic (all metrics in m); bias is omitted for the three local-datum drone benchmarks and DTM metrics are omitted for the four campaigns excluded from DTM validation.

Benchmark	Cells	Metric	DTM	P_5	P_{50}	P_{95}	Mean DSM	DSM σ_z
India Drone	522k	DRMSE	0.91	1.76	2.82	3.51	2.23	1.26
		NMAD	0.72	1.01	1.72	2.62	1.53	0.99
		Bias	—	—	—	—	—	—
3D Trees Drone	12k	DRMSE	3.99	7.88	7.71	7.98	6.66	3.37
		NMAD	2.56	5.17	5.21	4.23	4.62	2.68
		Bias	—	—	—	—	—	—
Global Drone	375k	DRMSE	2.05	2.83	3.76	4.10	3.05	1.45
		NMAD	1.48	1.86	2.53	2.76	2.16	0.94
		Bias	—	—	—	—	—	—
New Zealand	9.5M	DRMSE	4.31	4.16	4.20	4.77	3.92	1.55
		NMAD	1.76	1.55	1.52	1.84	1.50	0.53
		Bias	2.56	1.40	0.52	-0.15	0.55	-0.69
US NEON	60.9M	DRMSE	5.29	4.16	3.88	4.24	3.52	1.60
		NMAD	1.47	1.39	1.32	1.73	1.29	0.65
		Bias	1.23	1.03	-0.83	-2.85	-0.86	-1.38
Canada	4.8M	DRMSE	—	3.76	3.90	4.63	3.61	1.59
		NMAD	—	1.61	1.73	2.20	1.71	0.79
		Bias	—	-2.90	-4.79	-6.73	-4.80	-1.36
UK England	9.0M	DRMSE	2.47	3.07	2.58	2.76	2.33	1.29
		NMAD	1.25	1.20	1.20	1.45	1.17	0.38
		Bias	0.08	0.59	0.26	-0.25	0.22	-0.37
US Tropical	1.4M	DRMSE	—	1.27	1.43	1.89	1.33	0.66
		NMAD	—	0.66	0.82	1.10	0.78	0.32
		Bias	—	3.01	1.88	0.67	1.86	-0.79
Spain	16.5M	DRMSE	1.30	2.33	1.50	2.18	1.39	1.01
		NMAD	0.80	0.74	0.81	1.38	0.85	0.38
		Bias	0.75	0.99	0.77	0.05	0.66	-0.45
Brazil	1.1M	DRMSE	—	5.47	4.86	4.56	4.20	1.99
		NMAD	—	4.69	3.05	2.82	2.85	1.64
		Bias	—	3.40	-2.81	-5.91	-2.25	-3.18
Indonesia	1.9M	DRMSE	7.57	7.54	6.94	7.17	6.06	2.90
		NMAD	4.80	5.31	3.62	4.09	3.48	2.09
		Bias	9.42	7.11	0.13	-5.04	0.45	-4.17
Mozambique	8.8M	DRMSE	—	2.65	1.82	2.36	1.69	1.07
		NMAD	—	1.99	1.28	1.64	1.28	0.87
		Bias	—	3.48	1.15	-0.75	1.23	-1.41
Mean (Airborne)	114.9M	DRMSE	3.48	3.91	3.78	4.18	3.33	1.65
		NMAD	1.86	2.27	2.07	2.32	1.94	1.02
		Bias	2.81	2.01	-0.41	-2.33	-0.33	-1.53

Table E4. Validation against the 2025-epoch coordinates of 4071 international GNSS CORS stations, pooled globally and stratified by continent (Sect. 3.2.3). All metrics are in m, with the best model per metric in each row shown in bold.

Continent	Stations	Metric	GEM-15 DSM	Copernicus GLO-30	ALOS AW3D30	NASADEM
Global (All)	4071	DRMSE	**4.92**	5.80	5.66	6.55
		NMAD	4.20	**3.54**	3.85	4.74
		Bias	**-5.12**	-6.52	-5.40	-7.70
North America	1697	DRMSE	**4.41**	4.79	4.73	5.92
		NMAD	3.87	**2.95**	3.07	4.03
		Bias	-4.12	-5.26	**-3.86**	-6.65
Europe	1238	DRMSE	**5.34**	6.95	6.55	7.07
		NMAD	**4.13**	4.89	4.68	5.51
		Bias	**-7.29**	-9.32	-8.36	-10.21
Asia	527	DRMSE	**3.47**	3.83	3.81	5.66
		NMAD	3.00	**1.50**	2.62	3.22
		Bias	-6.03	**-5.08**	-5.11	-6.05
Oceania	305	DRMSE	**3.87**	4.62	4.25	5.92
		NMAD	**2.57**	3.19	2.81	4.66
		Bias	**-2.83**	-5.89	-4.31	-7.57
South America	228	DRMSE	**5.30**	5.99	6.05	6.91
		NMAD	**3.28**	4.17	4.21	5.67
		Bias	**-2.42**	-5.29	-3.47	-6.22
Africa	76	DRMSE	**4.30**	5.20	4.83	6.66
		NMAD	3.90	4.20	**3.72**	5.35
		Bias	**-3.02**	-5.34	-3.74	-6.65

Code and data availability

The GEM-15 dataset (v1) is openly available under the Creative Commons Attribution 4.0 International (CC BY 4.0) license at https://storage.googleapis.com/climate-and-sustainability/gem-15. To support both cloud-native geospatial workflows and direct bulk downloads, the dataset, code, and visualization tools are accessible through four channels: (1) Google Earth Engine Data Catalog, available as the public image collection projects/climate-and-sustainability/assets/gem-15_v1 (catalog page: https://developers.google.com/earth-engine/datasets/catalog/projects_climate-and-sustainability_assets_gem-15_v1); (2) Interactive Web Explorer, a browser-based Earth Engine App for side-by-side visual comparison of GEM-15 DSM, DTM, and 30 m baselines hosted at https://climate-and-sustainability.projects.earthengine.app/view/gem-15; (3) Google Cloud Storage (Cloud-Optimized GeoTIFFs), where the complete global set of $1^\circ \times 1^\circ$ UTM-projected COG tiles (https://storage.googleapis.com/climate-and-sustainability/gem-15) and SpatioTemporal Asset Catalog (STAC) metadata (https://storage.googleapis.com/climate-and-sustainability/gem-15/stac) are hosted in a public bucket configured with a permanent, no-deletion retention policy; and (4) Evaluation and Benchmarking Code, with scripts for reproducing the benchmark evaluations, tile-debiasing metrics, and figure visualizations available at https://github.com/google-research/google-research/tree/master/gem_15.

Author contributions. VB led the conceptualization, methodology, evaluation benchmark design, validation, formal analysis, and visualization. VB and TL developed and executed the global inference pipeline and dataset formatting. MN contributed to conceptualization, project direction, literature review, and methodological comparisons against existing global DEMs. CVA provided overall supervision and guidance on the formal analysis and performance evaluation of GEM-15. BA and JZ provided details on methodology and usage of the native DSMs and DTMs. VB and MN wrote the initial draft of the manuscript with contributions from TL, BA, and JZ, and all authors reviewed and edited the final manuscript.

Competing interests. The authors are employees of Google, which developed and publicly released the GEM-15 dataset described in this paper. The authors declare no other competing interests.

Acknowledgements. We thank Ori Lefkovitz and Joel Conkling for product leadership and support throughout the project; Veselin Dikov for leadership support and, together with Alex Wilson, manuscript review; Ivan Dryanovski, Kristi Greenbohl, Yongsung Kim, Steve Choi, and the broader Google Geo teams for the underlying satellite stereo infrastructure and dataset production; Tim Taylor and John Quintero for geospatial policy guidance; Kurt Schwehr for his elevation modeling expertise; Grey Nearing and Anna Michalak for domain feedback; and the Google Earth Engine team for dataset hosting. We also acknowledge Airbus Defence and Space and Maxar Technologies for commercial satellite imagery, Tech Mahindra Limited for commissioned UAV lidar benchmarks, and the open baseline DEM and reference data providers (ESA/DLR, JAXA, NASA/JPL, University of Bristol/Fathom, NASA/UMD GEDI, USGS 3DEP, NSF NEON, LINZ, UK Environment Agency, NRCan, Spain CNIG, NASA CMS/ORNL DAAC, 3D Trees, and NGL and international GNSS CORS networks). Generative AI

tools (Google Gemini) were used to assist with code development for the figures and with paper writing and reviews; the authors verified all outputs and take full responsibility for the content.

References

Batchu, V., Wilson, A., Peng, B., Elkin, C., Jain, U., Van Arsdale, C., Goroshin, R., and Gulshan, V.: Satellite Sunroof: High-res Digital Surface Models and Roof Segmentation for Global Solar Mapping, in: NeurIPS 2024 Workshop on Tackling Climate Change with Machine Learning, https://doi.org/10.48550/arXiv.2408.14400, 2024.

Baugh, C. A., Bates, P. D., Schumann, G., and Trigg, M. A.: SRTM vegetation removal and hydrodynamic modeling accuracy, Water Resources Research, 49, 5276–5289, https://doi.org/10.1002/wrcr.20412, 2013.

Beck, J., Wirt, B., Armston, J., Hofton, M., Luthcke, S., and Tang, H.: Global Ecosystem Dynamics Investigation (GEDI) Level 2 User Guide, Tech. Rep. Document Version 2.0, U.S. Geological Survey, Earth Resources Observation and Science Center (LP DAAC), Sioux Falls, South Dakota, USA, https://pubs.usgs.gov/publication/70270509, 2021.

Bielski, C., López-Vázquez, C., Grohmann, C. H., Guth, P. L., Hawker, L., Gesch, D., Trevisani, S., Herrera-Cruz, V., Riazanoff, S., Corseaux, A., Reuter, H. I., and Strobl, P.: Novel Approach for Ranking DEMs: Copernicus DEM Improves One Arc Second Open Global Topography, IEEE Transactions on Geoscience and Remote Sensing, 62, 1–22, https://doi.org/10.1109/TGRS.2024.3368015, 2024.

Boykov, Y., Veksler, O., and Zabih, R.: Fast Approximate Energy Minimization via Graph Cuts, IEEE Transactions on Pattern Analysis and Machine Intelligence, 23, 1222–1239, https://doi.org/10.1109/34.969114, 2001.

Brinck, K., Fischer, R., Groeneveld, J., Lehmann, S., Dantas De Paula, M., Pütz, S., Sexton, J. O., Song, D., and Huth, A.: High resolution analysis of tropical forest fragmentation and its impact on the global carbon cycle, Nature Communications, 8, 14 855, https://doi.org/10.1038/ncomms14855, 2017.

Cook, B. D., Corp, L. A., Nelson, R. F., Middleton, E. M., Morton, D. C., McCorkel, J. T., Masek, J. G., Ranson, K. J., Ly, V., and Montesano, P. M.: NASA Goddard's LiDAR, Hyperspectral and Thermal (G-LiHT) Airborne Imager, Remote Sensing, 5, 4045–4066, https://doi.org/10.3390/rs5084045, 2013.

Crippen, R., Buckley, S., Agram, P., Belz, E., Gurrola, E., Hensley, S., Kobrick, M., Lavalle, M., Martin, J., Neumann, M., Nguyen, Q., Rosen, P., Shimada, J., Simard, M., and Tung, W.: NASADEM Global Elevation Model: Methods and Progress, vol. XLI-B4, pp. 125–128, https://doi.org/10.5194/isprs-archives-XLI-B4-125-2016, 2016.

Department of Science and Technology, Government of India: Government announces liberalised guidelines for geo-spatial data, Press Information Bureau, Ministry of Science and Technology, New Delhi, India, https://www.pib.gov.in/Pressreleaseshare.aspx?PRID=1698196, 15 February 2021, 2021.

Department of Science and Technology, Government of India: National Geospatial Policy, 2022, The Gazette of India, Ministry of Science and Technology, New Delhi, India, https://dst.gov.in/geospatial-policy, notified 28 December 2022, 2022.

dos Santos, M. N., Keller, M. M., and Morton, D. C.: LiDAR Surveys over Selected Forest Research Sites, Brazilian Amazon, 2008–2018, ORNL DAAC, Oak Ridge, Tennessee, USA, https://doi.org/10.3334/ORNLDAAC/1644, 2019.

Dubayah, R., Blair, J. B., Goetz, S., Fatoyinbo, L., Hansen, M., Healey, S. P., Hofton, M., Hurtt, G., Kellner, J., Luthcke, S., Armston, J., Tang, H., Duncanson, L., Hancock, S., Jantz, P., Marselis, S., Patterson, P. L., Qi, W., and Silva, C.: The Global Ecosystem Dynamics Investigation: High-resolution laser ranging of the Earth's forests and topography, Science of Remote Sensing, 1, 100 002, https://doi.org/10.1016/j.srs.2020.100002, 2020.

Environment Agency: National LIDAR Programme, UK Defra Data Services Platform, https://environment.data.gov.uk/, 2022.

Esch, T., Brzoska, E., Dech, S., Leutner, B., Palacios-Lopez, D., Metz-Marconcini, A., Marconcini, M., Roth, A., and Zeidler, J.: World Settlement Footprint 3D – A first three-dimensional survey of the global building stock, Remote Sensing of Environment, 270, 112 877, https://doi.org/10.1016/j.rse.2021.112877, 2022.

European Space Agency: Copernicus DEM, https://doi.org/10.5270/ESA-c5d3d65, GLO-30, Version 2023_1, 2022.

Farr, T. G., Rosen, P. A., Caro, E., Crippen, R., Duren, R., Hensley, S., Kobrick, M., Paller, M., Rodriguez, E., Roth, L., Seal, D., Shaffer, S., Shimada, J., Umland, J., Werner, M., Oskin, M., Burbank, D., and Alsdorf, D.: The Shuttle Radar Topography Mission, Reviews of Geophysics, 45, RG2004, https://doi.org/10.1029/2005RG000183, 2007.

Fatoyinbo, L. and Trettin, C.: CMS: LiDAR Data for Mangrove Forests in the Zambezi River Delta, Mozambique, 2014, ORNL DAAC, Oak Ridge, Tennessee, USA, https://doi.org/10.3334/ORNLDAAC/1521, 2017.

Friedl, M. and Sulla-Menashe, D.: MCD12Q1 MODIS/Terra+Aqua Land Cover Type Yearly L3 Global 500m SIN Grid V006, NASA EOSDIS Land Processes Distributed Active Archive Center, https://doi.org/10.5067/MODIS/MCD12Q1.006, 2019.

Gallup, D., Frahm, J.-M., Mordohai, P., Yang, Q., and Pollefeys, M.: Real-time plane-sweeping stereo with multiple sweeping directions, in: 2007 IEEE Conference on Computer Vision and Pattern Recognition (CVPR), pp. 1–8, https://doi.org/10.1109/CVPR.2007.383245, 2007.

Gerberding, K., Vajna-Jehle, J., Lusk, D., Grüning, B., Kattenborn, T., Sperlich, M., Brede, B., Seifert, T., Scharinger, C., Greven, H., Nahrwold, L., Seiler, J., Reiterer, A., and Frey, J.: 3Dtrees.earth: Technical Infrastructure for FAIR Forest LiDAR Data Management and Analysis, in: Publikationen der Deutschen Gesellschaft für Photogrammetrie, Fernerkundung und Geoinformation (DGPF), edited by Kersten, T. P. and Tilly, N., vol. 34, https://freidok.uni-freiburg.de/data/281637, 2026.

Gevaert, C. M., Persello, C., Nex, F., and Vosselman, G.: A deep learning approach to DTM extraction from imagery using rule-based training labels, ISPRS Journal of Photogrammetry and Remote Sensing, 142, 106–123, https://doi.org/10.1016/j.isprsjprs.2018.06.001, 2018.

Gorelick, N., Hancher, M., Dixon, M., Ilyushchenko, S., Thau, D., and Moore, R.: Google Earth Engine: Planetary-scale geospatial analysis for everyone, Remote Sensing of Environment, 202, 18–27, https://doi.org/10.1016/j.rse.2017.06.031, 2017.

Grimmond, C. S. B. and Oke, T. R.: Aerodynamic Properties of Urban Areas Derived from Analysis of Surface Form, Journal of Applied Meteorology, 38, 1262–1292, https://doi.org/10.1175/1520-0450(1999)038<1262:APOUAD>2.0.CO;2, 1999.

Grodecki, J. and Dial, G.: Block Adjustment of High-Resolution Satellite Images Described by Rational Polynomials, Photogrammetric Engineering & Remote Sensing, 69, 59–68, https://doi.org/10.14358/PERS.69.1.59, 2003.

Haddad, N. M., Brudvig, L. A., Clobert, J., Davies, K. F., Gonzalez, A., Holt, R. D., Lovejoy, T. E., Sexton, J. O., Austin, M. P., Collins, C. D., et al.: Habitat fragmentation and its lasting impact on Earth's ecosystems, Science Advances, 1, e1500 052, https://doi.org/10.1126/sciadv.1500052, 2015.

Hansen, M. C., Potapov, P. V., Moore, R., Hancher, M., Turubanova, S. A., Tyukavina, A., Thau, D., Stehman, S. V., Goetz, S. J., Loveland, T. R., Kommareddy, A., Egorov, A., Chini, L., Justice, C. O., and Townshend, J. R. G.: High-Resolution Global Maps of 21st-Century Forest Cover Change, Science, 342, 850–853, https://doi.org/10.1126/science.1244693, 2013.

Hawker, L., Bates, P., Neal, J., and Rougier, J.: Perspectives on Digital Elevation Model (DEM) Simulation for Flood Modeling in the Absence of a High-Accuracy Open Access Global DEM, Frontiers in Earth Science, 6, 233, https://doi.org/10.3389/feart.2018.00233, 2018.

Hawker, L., Uhe, P., Paulo, L., Sosa, J., Savage, J., Sampson, C., and Neal, J.: A 30 m global map of elevation with forests and buildings removed, Environmental Research Letters, 17, 024 016, https://doi.org/10.1088/1748-9326/ac4d4f, 2022.

He, K., Zhang, X., Ren, S., and Sun, J.: Deep Residual Learning for Image Recognition, in: 2016 IEEE Conference on Computer Vision and Pattern Recognition (CVPR), pp. 770–778, https://doi.org/10.1109/CVPR.2016.90, 2016.

Ho, Y.-F., Grohmann, C. H., Lindsay, J., Reuter, H. I., Parente, L., Witjes, M., and Hengl, T.: GEDTM30: global ensemble digital terrain model at 30 m and derived multiscale terrain variables, PeerJ, 13, e19 673, https://doi.org/10.7717/peerj.19673, 2025.

Hodgson, M. E. and Bresnahan, P.: Accuracy of Airborne LiDAR-Derived Elevation: Empirical Assessment and Error Budget, Photogrammetric Engineering & Remote Sensing, 70, 331–339, https://doi.org/10.14358/PERS.70.3.331, 2004.

Höhle, J. and Höhle, M.: Accuracy assessment of digital elevation models by means of robust statistical methods, ISPRS Journal of Photogrammetry and Remote Sensing, 64, 398–406, https://doi.org/10.1016/j.isprsjprs.2009.02.003, 2009.

Howat, I. M., Porter, C., Smith, B. E., Noh, M.-J., and Morin, P.: The Reference Elevation Model of Antarctica, The Cryosphere, 13, 665–674, https://doi.org/10.5194/tc-13-665-2019, 2019.

Instituto Geográfico Nacional: Plan Nacional de Ortofotografía Aérea, Proyecto PNOA-LiDAR, Centro Nacional de Información Geográfica (CNIG), Madrid, Spain, https://pnoa.ign.es/web/portal/pnoa-lidar/presentacion, 2024.

Johnston, G., Riddell, A., and Hausler, G.: The International GNSS Service, in: Springer Handbook of Global Navigation Satellite Systems, edited by Teunissen, P. J. G. and Montenbruck, O., pp. 967–982, Springer International Publishing, Cham, https://doi.org/10.1007/978-3-319-42928-1_33, 2017.

Kampe, T. U., Johnson, B. R., Kuester, M. A., and Keller, M.: NEON: the first continental-scale ecological observatory with airborne remote sensing of vegetation canopy biochemistry and structure, Journal of Applied Remote Sensing, 4, 043 510, https://doi.org/10.1117/1.3361375, 2010.

Krieger, G., Moreira, A., Fiedler, H., Hajnsek, I., Werner, M., Younis, M., and Zink, M.: TanDEM-X: A Satellite Formation for High-Resolution SAR Interferometry, IEEE Transactions on Geoscience and Remote Sensing, 45, 3317–3341, https://doi.org/10.1109/TGRS.2007.900693, 2007.

Kulp, S. A. and Strauss, B. H.: New elevation data triple estimates of global vulnerability to sea-level rise and coastal flooding, Nature Communications, 10, 4844, https://doi.org/10.1038/s41467-019-12808-z, 2019.

Land Information New Zealand: New Zealand Lidar 1 Meter DEM, Distributed by OpenTopography and LINZ, https://doi.org/10.5069/G9ZK5DW0, 2025.

Lang, N., Jetz, W., Schindler, K., and Wegner, J. D.: A high-resolution canopy height model of the Earth, Nature Ecology & Evolution, 7, 1778–1789, https://doi.org/10.1038/s41559-023-02206-6, 2023.

Laurance, W. F., Laurance, S. G., Ferreira, L. V., Rankin-de Merona, J. M., Gascon, C., and Lovejoy, T. E.: Biomass Collapse in Amazonian Forest Fragments, Science, 278, 1117–1118, https://doi.org/10.1126/science.278.5340.1117, 1997.

Lehner, B., Verdin, K., and Jarvis, A.: New global hydrography derived from spaceborne elevation data, Eos, Transactions American Geophysical Union, 89, 93–94, https://doi.org/10.1029/2008EO100001, 2008.

Leitold, V., Morton, D. C., Martinuzzi, S., Paynter, I., Uriarte, M., Keller, M., Ferraz, A., Cook, B. D., Corp, L., and González, G.: Canopy damage and recovery following Hurricane Maria using multitemporal lidar data, Mar/2017–Mar/2020, Puerto Rico, NASA Carbon Monitoring System / NGEE Tropics, https://doi.org/10.15486/ngt/1797399, 2021.

Lemoine, F. G., Kenyon, S. C., Factor, J. K., Trimmer, R. G., Pavlis, N. K., Chinn, D. S., Cox, C. M., Klosko, S. M., Luthcke, S. B., Torrence, M. H., Wang, Y. M., Williamson, R. G., Pavlis, E. C., Rapp, R. H., and Olson, T. R.: The Development of the Joint NASA GSFC and the National Imagery and Mapping Agency (NIMA) Geopotential Model EGM96, Tech. Rep. NASA/TP-1998-206861, NASA Goddard Space Flight Center, Greenbelt, Maryland, USA, https://ntrs.nasa.gov/citations/19980218814, 1998.

Lindsay, J. B.: The practice of DEM stream burning revisited, Earth Surface Processes and Landforms, 41, 658–668, https://doi.org/10.1002/esp.3888, 2016.

Liu, A., Cheng, X., and Chen, Z.: Performance evaluation of GEDI and ICESat-2 laser altimeter data for terrain and canopy height retrievals, Remote Sensing of Environment, 264, 112 571, https://doi.org/10.1016/j.rse.2021.112571, 2021.

Markus, T., Neumann, T., Martino, A., Abdalati, W., Brunt, K., Csatho, B., Farrell, S., Fricker, H., Gardner, A., Harding, D., Jasinski, M., Kwok, R., Magruder, L., Lubin, D., Luthcke, S., Morison, J., Nelson, R., Neuenschwander, A., Palm, S., Popescu, S., Shum, C. K., Schutz, B. E., Smith, B., Yang, Y., and Zwally, J.: The Ice, Cloud, and land Elevation Satellite-2 (ICESat-2): Science requirements, concept, and implementation, Remote Sensing of Environment, 190, 260–273, https://doi.org/10.1016/j.rse.2016.12.029, 2017.

Maus, V., Giljum, S., Gutschlhofer, J., da Silva, D. M., Probst, M., Gass, S. L. B., Luckeneder, S., Lieber, M., and McCallum, I.: A global-scale data set of mining areas, Scientific Data, 7, 289, https://doi.org/10.1038/s41597-020-00624-w, 2020.

Melendy, L., Hagen, S., Sullivan, F., Pearson, T., Walker, S., Ellis, P., KUSTIYO, Sambodo, K., Roswintiarti, O., Hanson, M., Klassen, A., Palace, M., Braswell, B., Delgado, G., Saatchi, S., and Ferraz, A.: CMS: LiDAR-derived Canopy Height, Elevation for Sites in Kalimantan, Indonesia, 2014, ORNL DAAC, Oak Ridge, Tennessee, USA, https://doi.org/10.3334/ORNLDAAC/1540, 2017.

NASA JPL: NASADEM Merged DEM Global 1 arc second V001, NASA EOSDIS Land Processes Distributed Active Archive Center, https://doi.org/10.5067/MEaSUREs/NASADEM/NASADEM_HGT.001, 2020.

Natural Resources Canada: High Resolution Digital Elevation Model of Canada, Government of Canada / OpenTopography, https://doi.org/10.5069/G9R20ZKN, 2025.

NEON: Elevation – LiDAR (DP3.30024.001), RELEASE-2026, NEON Data Portal, https://doi.org/10.48443/sxrt-ne87, 2026.

Neuenschwander, A. and Pitts, K.: The ATL08 land and vegetation product for the ICESat-2 Mission, Remote Sensing of Environment, 221, 247–259, https://doi.org/10.1016/j.rse.2018.11.005, 2019.

Noh, M.-J. and Howat, I. M.: Automated stereo-photogrammetric DEM generation at high latitudes: Surface Extraction with TIN-based Search-space Minimization (SETSM) validation and demonstration over glaciated regions, GIScience & Remote Sensing, 52, 198–217, https://doi.org/10.1080/15481603.2015.1008621, 2015.

Pavlis, N. K., Holmes, S. A., Kenyon, S. C., and Factor, J. K.: The development and evaluation of the Earth Gravitational Model 2008 (EGM2008), Journal of Geophysical Research: Solid Earth, 117, B04 406, https://doi.org/10.1029/2011JB008916, 2012.

Porter, C., Morin, P., Howat, I., Noh, M.-J., Bates, B., Peterman, K., Keesey, S., Schlenk, M., Gardiner, J., Tomko, K., Willis, M., Kelleher, C., Cloutier, M., Husby, E., Foga, S., Nakamura, H., Platson, M., Wethington, M., Williamson, C., Bauer, G., Enos, J., Arnold, G., Kramer, W., Becker, P., Doshi, A., D'Souza, C., Cummens, P., Laurier, F., and Bojesen, M.: ArcticDEM, Version 3, Harvard Dataverse [data set], https://doi.org/10.7910/DVN/OHHUKH, 2018.

Potapov, P., Li, X., Hernandez-Serna, A., Tyukavina, A., Hansen, M. C., Kommareddy, A., Pickens, A., Turubanova, S., Tang, H., Silva, C. E., Armston, J., Dubayah, R., Blair, J. B., and Hofton, M.: Mapping global forest canopy height through integration of GEDI and Landsat data, Remote Sensing of Environment, 253, 112 165, https://doi.org/10.1016/j.rse.2020.112165, 2021.

Puliti, S., Pearse, G., Surový, P., Wallace, L., Hollaus, M., Wielgosz, M., and Astrup, R.: FOR-instance: a UAV laser scanning benchmark dataset for semantic and instance segmentation of individual trees, arXiv preprint arXiv:2309.01279, https://doi.org/10.48550/arXiv.2309.01279, 2023.

Reichenbach, P., Rossi, M., Malamud, B. D., Mihir, M., and Guzzetti, F.: A review of statistically-based landslide susceptibility models, Earth-Science Reviews, 180, 60–91, https://doi.org/10.1016/j.earscirev.2018.03.001, 2018.

Rizzoli, P., Martone, M., Gonzalez, C., Wecklich, C., Borla Tridon, D., Bräutigam, B., Bachmann, M., Schulze, D., Fritz, T., Huber, M., Wessel, B., Krieger, G., Zink, M., and Moreira, A.: Generation and performance assessment of the global TanDEM-X digital elevation model, ISPRS Journal of Photogrammetry and Remote Sensing, 132, 119–139, https://doi.org/10.1016/j.isprsjprs.2017.08.008, 2017.

Ronneberger, O., Fischer, P., and Brox, T.: U-Net: Convolutional Networks for Biomedical Image Segmentation, in: Medical Image Computing and Computer-Assisted Intervention – MICCAI 2015, vol. 9351 of *Lecture Notes in Computer Science*, pp. 234–241, Springer International Publishing, https://doi.org/10.1007/978-3-319-24574-4_28, 2015.

Sampson, C. C., Smith, A. M., Bates, P. D., Neal, J. C., Alfieri, L., and Freer, J. E.: A high-resolution global flood hazard model, Water Resources Research, 51, 7358–7381, https://doi.org/10.1002/2015WR016954, 2015.

Schubert, J. E. and Sanders, B. F.: Building treatments for urban flood inundation models and implications for predictive skill and modeling efficiency, Advances in Water Resources, 41, 49–64, https://doi.org/10.1016/j.advwatres.2012.02.012, 2012.

Schutz, B. E., Zwally, H. J., Shuman, C. A., Hancock, D., and DiMarzio, J. P.: Overview of the ICESat Mission, Geophysical Research Letters, 32, L21S01, https://doi.org/10.1029/2005GL024009, 2005.

Seto, K. C., Güneralp, B., and Hutyra, L. R.: Global forecasts of urban expansion to 2030 and direct impacts on biodiversity and carbon pools, Proceedings of the National Academy of Sciences, 109, 16 083–16 088, https://doi.org/10.1073/pnas.1211658109, 2012.

Shean, D. E., Alexandrov, O., Moratto, Z. M., Smith, B. E., Joughin, I. R., Porter, C., and Morin, P.: An automated, open-source pipeline for mass production of digital elevation models (DEMs) from very-high-resolution commercial stereo satellite imagery, ISPRS Journal of Photogrammetry and Remote Sensing, 116, 101–117, https://doi.org/10.1016/j.isprsjprs.2016.03.012, 2016.

Simard, M., Denbina, M., Marshak, C., and Neumann, M.: A global evaluation of radar-derived digital elevation models: SRTM, NASADEM, and GLO-30, Journal of Geophysical Research: Biogeosciences, 129, e2023JG007 672, https://doi.org/10.1029/2023JG007672, 2024.

Sithole, G. and Vosselman, G.: Experimental comparison of filter algorithms for bare-Earth extraction from airborne laser scanning point clouds, ISPRS Journal of Photogrammetry and Remote Sensing, 59, 85–101, https://doi.org/10.1016/j.isprsjprs.2004.05.004, 2004.

Snay, R. A. and Soler, T.: Continuously Operating Reference Station (CORS): History, Applications, and Future Enhancements, Journal of Surveying Engineering, 134, 95–104, https://doi.org/10.1061/(ASCE)0733-9453(2008)134:4(95), 2008.

Stewart, I. D. and Oke, T. R.: Local Climate Zones for Urban Temperature Studies, Bulletin of the American Meteorological Society, 93, 1879–1900, https://doi.org/10.1175/BAMS-D-11-00019.1, 2012.

Stoker, J. and Miller, B.: The Accuracy and Consistency of 3D Elevation Program Data: A Systematic Analysis, Remote Sensing, 14, 940, https://doi.org/10.3390/rs14040940, 2022.

Sulla-Menashe, D., Gray, J. M., Abercrombie, S. P., and Friedl, M. A.: Hierarchical mapping of annual global land cover 2001 to present: The MODIS Collection 6 Land Cover product, Remote Sensing of Environment, 222, 183–194, https://doi.org/10.1016/j.rse.2018.12.013, 2019.

Tadono, T., Takaku, J., Tsutsui, K., Oda, F., and Nagai, H.: Status of "ALOS World 3D (AW3D)" Global DSM Generation, in: 2015 IEEE International Geoscience and Remote Sensing Symposium (IGARSS), pp. 3822–3825, https://doi.org/10.1109/IGARSS.2015.7326657, 2015.

Takaku, J., Tadono, T., and Tsutsui, K.: Generation of High Resolution Global DSM from ALOS PRISM, The International Archives of the Photogrammetry, Remote Sensing and Spatial Information Sciences, XL-4, 243–248, https://doi.org/10.5194/isprsarchives-XL-4-243-2014, 2014.

Tang, H., Stoker, J., Luthcke, S., Armston, J., Lee, K., Blair, B., and Hofton, M.: Evaluating and mitigating the impact of systematic geolocation error on canopy height measurement performance of GEDI, Remote Sensing of Environment, 291, 113 571, https://doi.org/10.1016/j.rse.2023.113571, 2023.

Tao, C. V. and Hu, Y.: Use of the Rational Function Model for Image Rectification, Canadian Journal of Remote Sensing, 27, 593–602, https://doi.org/10.1080/07038992.2001.10854900, 2001.

Tolan, J., Yang, H.-I., Nosarzewski, B., Couairon, G., Vo, H. V., Brandt, J., Spore, J., Majumdar, S., Haziza, D., Vamaraju, J., Moutakanni, T., Bojanowski, P., Johns, T., White, B., Tiecke, T., and Couprie, C.: Very high resolution canopy height maps from RGB imagery using self-supervised vision transformer and convolutional decoder trained on aerial LiDAR, Remote Sensing of Environment, 300, 113 888, https://doi.org/10.1016/j.rse.2023.113888, 2024.

Uuemaa, E., Ahi, S., Montibeller, B., Muru, M., and Kmoch, A.: Vertical Accuracy of Freely Available Global Digital Elevation Models (ASTER, AW3D30, MERIT, TanDEM-X, SRTM, and NASADEM), Remote Sensing, 12, 3482, https://doi.org/10.3390/rs12213482, 2020.

Wessel, B., Huber, M., Wohlfart, C., Marschalk, U., Kosmann, D., and Roth, A.: Accuracy assessment of the global TanDEM-X Digital Elevation Model with GPS data, ISPRS Journal of Photogrammetry and Remote Sensing, 139, 171–182, https://doi.org/10.1016/j.isprsjprs.2018.02.017, 2018.

Yamazaki, D., Ikeshima, D., Tawatari, R., Yamaguchi, T., O'Loughlin, F., Neal, J. C., Sampson, C. C., Kanae, S., and Bates, P. D.: A high-accuracy map of global terrain elevations, Geophysical Research Letters, 44, 5844–5853, https://doi.org/10.1002/2017GL072874, 2017.

Yamazaki, D., Ikeshima, D., Sosa, J., Bates, P. D., Allen, G. H., and Pavelsky, T. M.: MERIT Hydro: A High-Resolution Global Hydrography Map Based on Latest Topography Dataset, Water Resources Research, 55, 5053–5073, https://doi.org/10.1029/2019WR024873, 2019.

Zanaga, D., Van De Kerchove, R., Daems, D., De Keersmaecker, W., Brockmann, C., Kirches, G., Wevers, J., Cartus, O., Santoro, M., Fritz, S., Lesiv, M., Herold, M., Tsendbazar, N.-E., Xu, P., Ramoino, F., and Arino, O.: ESA WorldCover 10 m 2021 v200, Zenodo [data set], https://doi.org/10.5281/zenodo.7254221, 2022.

Zhang, W., Qi, J., Wan, P., Wang, H., Xie, D., Wang, X., and Yan, G.: An Easy-to-Use Airborne LiDAR Data Filtering Method Based on Cloth Simulation, Remote Sensing, 8, 501, https://doi.org/10.3390/rs8060501, 2016.

Zwally, H. J., Schutz, B., Abdalati, W., Abshire, J., Bentley, C., Brenner, A., Bufton, J., Dezio, J., Hancock, D., Harding, D., Herring, T., Minster, B., Quinn, K., Palm, S., Spinhirne, J., and Thomas, R.: ICESat's laser measurements of polar ice, atmosphere, ocean, and land, Journal of Geodynamics, 34, 405–445, https://doi.org/10.1016/S0264-3707(02)00042-X, 2002.